A Revised Cooling and Extensional Exhumation History for the Harrison Pass Pluton, Southern Ruby Mountains Metamorphic Core Complex, Elko County, Nevada

Allen J. McGrew*
Department of Geology, The University of Dayton, Dayton, OH
James Metcalf
University of Colorado Boulder, Department of Geological Sciences, Boulder, CO

ABSTRACT

A key question in the tectonic evolution of the Sevier orogenic belt of the western U.S. Cordillera is when and why the overthickened crust of the hinterland plateau began to collapse giving rise to the modern extensional tectonic regime. Delineating the exhumation history of the Ruby Mountains, East Humboldt Range and Wood Hills metamorphic core complex (REHW) of Elko County, Nevada offers important evidence bearing on this question. Recent work from the northern REHW records a three-phase extensional history: (1) ~15–20 km of Late Eocene extension, (2) a second pulse of extension of similar rate and magnitude beginning in the late Oligocene or early Miocene (by 21 Ma) and continuing to approximately 11 Ma, and (3) the Basin-and-Range extensional regime continuing at reduced rate to today. In contrast, previous work from the Harrison Pass area in the southern REHW does not recognize an imprint from the Late Eocene phase of extension, and places the onset of the second extensional phase after ~17 Ma. New intermediate closure temperature thermochronology from the Harrison Pass pluton indicates that it remained at significant depth until at least ~25 Ma, severely limiting any possible Late Eocene to early Oligocene extension, consistent with previous interpretations. However, the new results challenge the previously proposed post-17 Ma onset for extension at Harrison Pass. New, intermediate closure temperature (U-Th)/He titanite and zircon ages from the eastern half of the pluton almost entirely predate 17 Ma and instead support an extensional onset bracketed between the Early Miocene (21 Ma) and the late Oligocene (25 Ma). Integrating potassium feldspar $^{40}Ar/^{39}Ar$ multi-diffusion domain modeling with the lower closure temperature thermochronometric systems reveals an inflection to faster cooling rates after ~25 Ma and further supports this inference. Nevertheless, all but the farthest east and structurally shallowest of the samples also show a second inflection point at ~17 Ma. We argue that previously reported apatite fission track and apatite (U-Th)/He data captured this post-17.5 Ma reacceleration event but missed the earlier, late Oligocene-early Miocene extension recorded by the higher temperature thermochronometers. The latest Oligocene to early Miocene extensional phase correlates with extensional events reported from southern Nevada and Arizona that may relate to the relaxation of contractional boundary conditions during the early evolution of the San Andreas margin. However, the post-17.5 Ma resurgence in extension probably correlates with large-scale crustal weakening across the northern Basin and Range province attending the arrival of the Yellowstone thermal plume.

Key Words: Ruby Mountains, Extension, Thermochronology, Core Complex

*E-mail: amcgrew1@udayton.edu

INTRODUCTION

The timing, pace, mechanism, magnitude and kinematic evolution of extension are fundamental issues throughout the Basin and Range province (e.g., Colgan and Henry, 2009; Henry and others, 2011). The most deeply exhumed terrains—the metamorphic core complexes—figure prominently in efforts to delineate the extensional history. With this paper we apply low to intermediate temperature thermochronometry to better resolve the extensional history of the southern part of the most deeply exhumed metamorphic terrain of the northern Basin and Range province—the Ruby Mountains-East Humboldt Range-Wood Hills metamorphic core complex (REHW) in Figures 1 and 2) (Howard, 1980; Snoke, 1980; Snoke and Miller, 1988; Snoke and others, 1990; Snoke and others, 1997; McGrew and others, 2000; Sullivan and Snoke, 2007).

Geologic Setting

The REHW is the farthest west and most deeply exhumed of the iconic metamorphic core complexes of the northeastern Great Basin—the others being the Snake Range and the Albion-Raft River-Grouse Creek Ranges (Coney, 1980; Howard, 2003; Sullivan and Snoke, 2007). Like the others, the REHW exhibits the classic definitive features of a metamorphic core complex: a high-grade metamorphic and plutonic core roofed by a well-developed extensional mylonitic shear zone overprinted by a low-angle detachment fault that is in turn overlain by a complexly normal faulted and brittlely attenuated superstructure of upper crustal sedimentary strata and syntectonic deposits. The Ruby Mountains-East Humboldt Range shear zone and detachment fault extends over 100 km SSW from the northern end of the East Humboldt Range to the southern Ruby Mountains, and exhibits dominant top-to-WNW normal-sense shear along its entire length (Sullivan and Snoke, 2007) (Figures 1 and 2).

The southern part of the Ruby Mountains of interest here is dominated by the Harrison Pass pluton—an approximately 10 km diameter stock emplaced at upper crustal levels into the transition zone between low-grade to non-metamorphic sedimentary strata to its south and the high-grade migmatitic core of the REHW to its north (Kistler and others, 1981; Hudec, 1992; Burton, 1997; Barnes and others, 2001). In contrast with areas farther north in the REHW, the migmatitic core immediately north of the Harrison Pass pluton was constructed primarily in the Late Jurassic rather than the Late Cretaceous. It was tectonically buried at that time to pressures of ~4.5 kbar (paleodepths of ~18 km, approximately 1.5 times stratigraphic depth) (Hudec, 1992; Jones, 1999). The mechanism of tectonic burial of these rocks remains unclear and somewhat controversial, but a number of complex thrust systems are discontinuously exposed in the Piñon Range to the west, including western facies rocks of the Roberts Mountains allochthon (Johnson and Pendergast, 1981; Trexler and others, 2004). Though commonly interpreted to have been emplaced during the Late Devonian to Mississippian, Ketner (1998) argues for complex and widespread overprinting and reactivation of the Antler belt from Late Jurassic onward, and a number of workers have documented evidence of significant Middle to Late Jurassic shortening—the "Elko Orogeny" (e.g., Thorman and Peterson, 2003). However, regardless of whether and how much tectonic burial there may have been on the north side of the Harrison Pass pluton, there appears to be little evidence for pre-extensional tectonic burial from Harrison Pass south. It appears likely that the Harrison Pass pluton was emplaced into the core of a broad, gentle pre-existing arch, the Rattlesnake Mountain anticline (Burton, 1997) that may correlate with the Illipah anticline of the Eastern Nevada fold belt (Long, 2015).

Despite the evidence of pre-Cenozoic deformation, structural relief east of the Roberts Mountains allochthon was modest – no more than 3 km based on the Mississippian to Jurassic ages of the rocks underlying the basal Paleogene unconformity (Armstrong, 1968; Gans and Miller, 1983; Long, 2012). This observation is reinforced locally by the preservation of rocks as young as Triassic in both the footwall of the Medicine Range to the east of the Ruby Mountains and in the upper plate exposed in the Piñon Range to the west (Colgan and others, 2010). Furthermore, the preservation of Mesozoic apatite (U-Th)/He (AHe) and apatite fission track (AFT) ages from the Medicine Mountains also precludes substantial Paleogene unroofing. Since the ranges to the east of the southern Ruby Mountains show no evidence of major westward-dipping normal faults that could potentially correlate with the Ruby detachment system, the "breakaway zone" where the Ruby detachment fault daylighted must have been between the southern Ruby Mountains and the Medicine Mountains/Maverick Springs Range—no more than ~8 km ESE of the upper contact of the pluton. This severely limits both the depth of burial of the pluton and the dip of the detachment (Figure 2).

Adding to the above constraints, seismic stratigraphy and numerous well log records in Huntington Valley indicate that the hanging wall strata that were displaced from the roof of the pluton also preserve Pennsylvanian and possibly younger strata underlying the basal Paleogene unconformity (Figure 2) (Satarugsa and Johnson, 2000; Hess and others, 2011). The Paleogene strata overlying the unconformity have traditionally been assigned to the Elko and Indian Wells Formations, but recently acquired U-Pb detrital zircon geochronology has led to a reinterpretation, with most of the Indian Wells formation reassigned to the lower Humboldt Formation, and only the lower ~1 km being assigned to the Late Eocene tuff of Dixie Creek (Lund Snee and Miller, 2015; Lund Snee and others, 2016).

Barnes and others (2001) estimate emplacement pressures for the pluton itself of approximately 3 kbar, approximately equal to estimated stratigraphic depths. The south side of the pluton consists of a low-grade (in the west) to unmetamorphosed Cambrian to Mississippian sedimentary sequence dipping moderately eastward and locally cut by the gently west-dipping Ruby Mountains detachment carrying moderately East-dipping syntectonic strata of the Humboldt Formation in its hanging wall (Figure 2). The pluton consists of at least three major phases intruded into the upper

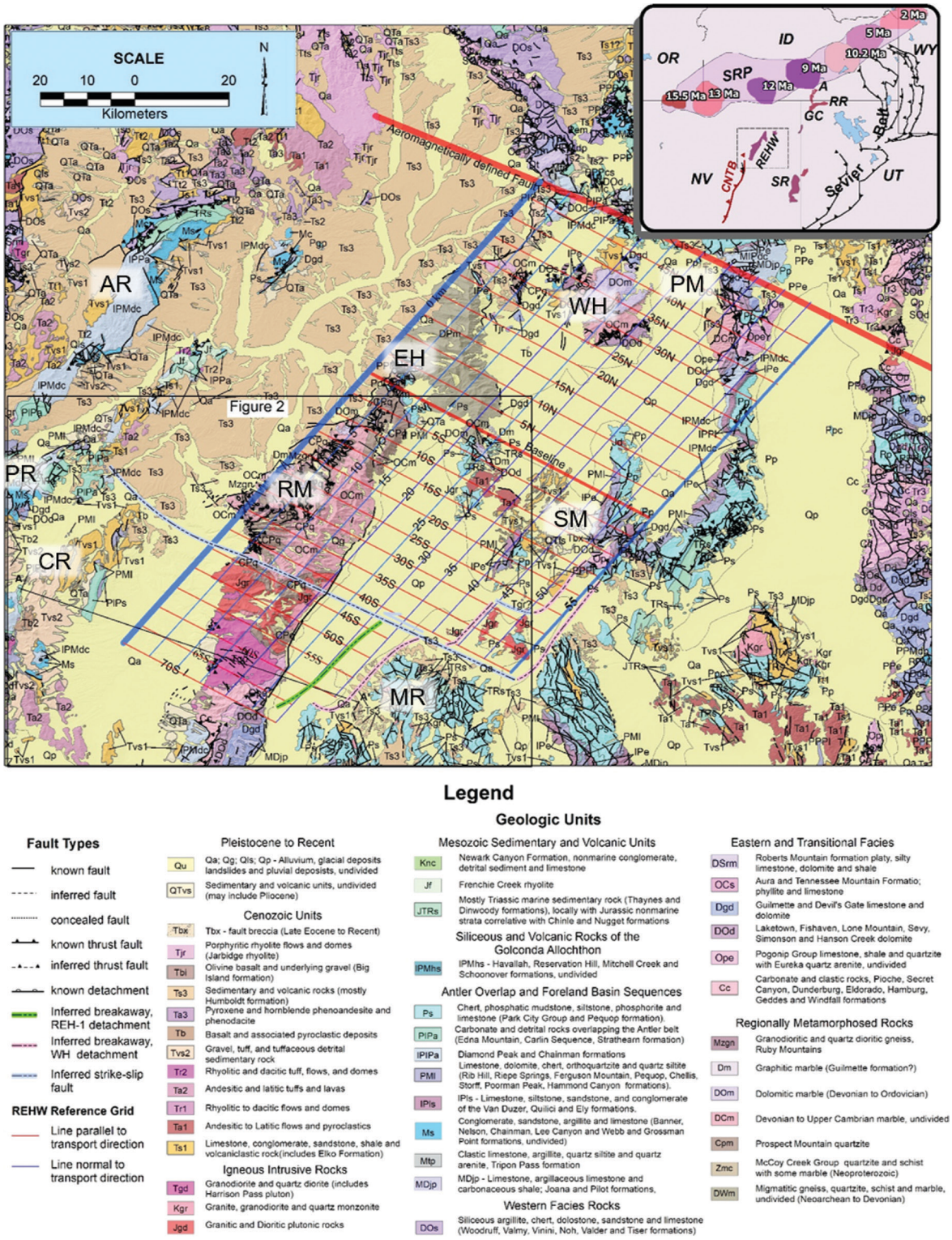

Figure 1. Regional geologic map of the Ruby Mountains—East Humboldt Range— Wood Hills Metamorphic core complex (REHW) (modified from Coats, 1987). Inset shows regional tectonic setting relative to the Snake River Plain (SRP) and calderas (with approximate ages) of the Yellowstone Hotspot track (Camp and others, 2015), Sevier orogenic belt, the Central Nevada thrust belt (CNTB), and the Snake Range (SR), Albion Range (A), Raft River (RR), and Grouse Creek (GC) metamorphic core complexes. Area of Figure 2 outlined by box in southwest quarter of main figure. Note 5 km square reference grid extending from the REHW baseline along the west flank of the northern REHW; red lines parallel to inferred tectonic transport direction (approximately 300°) whereas blue lines represent approximate paleodepth isolines. Mountain ranges abbreviated as follows: AR—Adobe Range; PR—Piñon Range; CR—Cedar Ridge, RM—Ruby Mountains, MR—northern Maverick Springs Range and Medicine Range; SM—Spruce Mountain; PM—Pequop Mountains; WH—Wood Hills; EH—East Humboldt Range.

middle crust between 38.1 ± 0.4 and 36.5 ± 0.2 Ma (Wright and Snoke, 1993; Barnes and others, 2001; Colgan and others, 2010).

Previous Work and Research Objectives

The new results presented below complement and build on numerous previously reported results collected and/or synthesized by Colgan and others (2010), although some of the older work comes with multi-million year uncertainties (Reese, 1986, Burton, 1997). In addition, a substantial data set of legacy biotite K-Ar (Kistler and others, 1981) and biotite $^{40}Ar/^{39}Ar$ (BtAr) dates also exists and records a well-developed WNW-younging apparent age gradient from ~36 Ma in the SE to ~25 Ma in the NW (Kistler and others, 1981; Colgan and others, 2010).

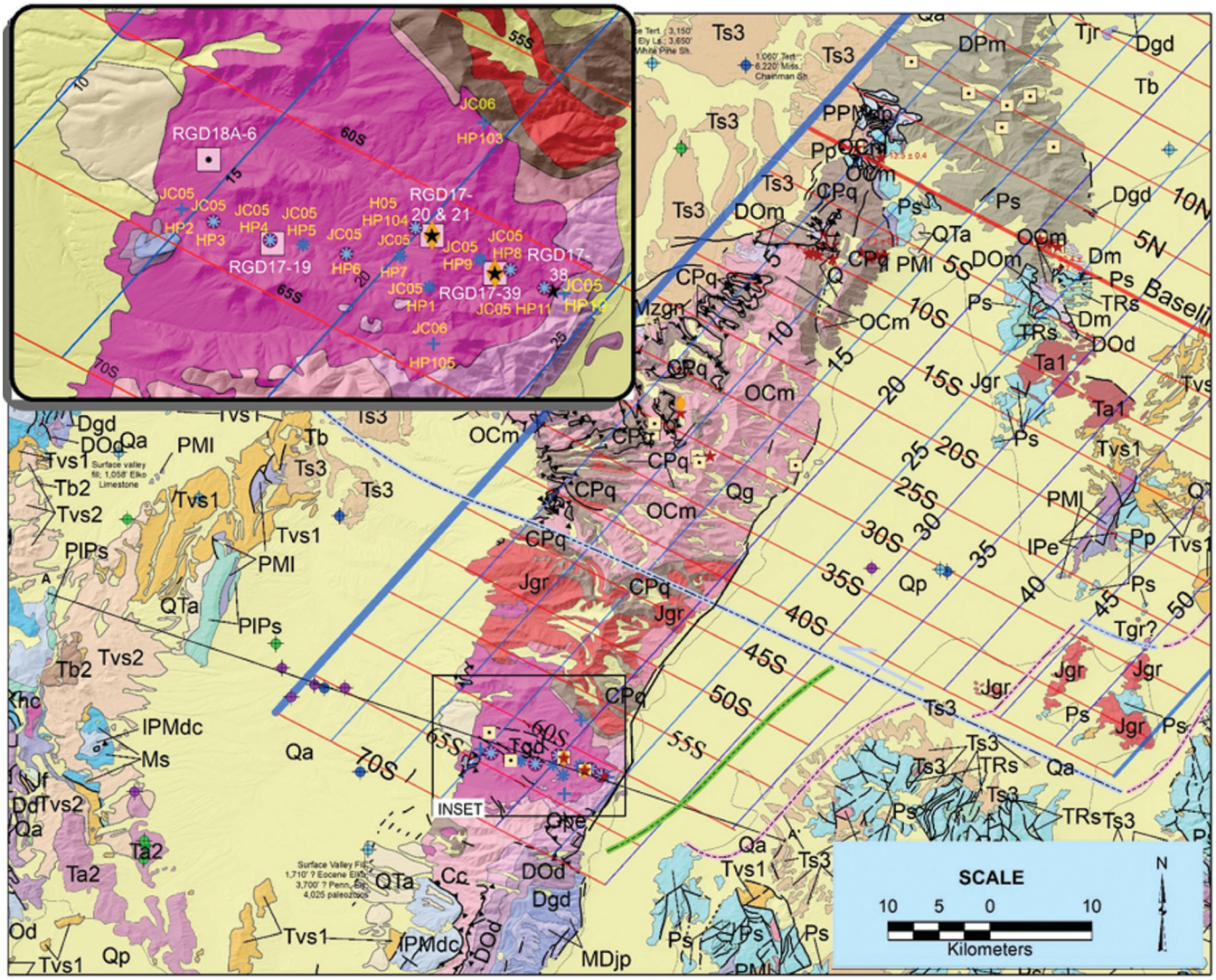

Figure 2. Generalized geologic map of the southern REHW and adjacent areas (after Coats, 1987) with inset locating sample localities from this study and from Colgan and others (2010). Rock units and REHW grid as indicated in legend of Figure 1.

Research Objective

Previous work offers only a few zircon fission track (ZFT) apparent ages (Reese, 1986) to fill in the ~200°C gap in closure temperatures between the BtAr and AFT systems—nominally ~325°C for BtAr (Harrison and others, 1985) and ~120°C for AFT (Ketcham and others, 1999). The chief purpose of this paper is to augment the pre-existing results with newly collected intermediate closure temperature systems—i.e., $^{40}Ar/^{39}Ar$ potassium feldspar (KfAr) ($T_c \approx$ 150–350°C), (U-Th)/He titanite (TnHe) ($T_c \approx$ 210°C), and (U-Th)/He zircon (ZHe) ($T_c \approx$ 180°C). We emphasize that the nominal closure temperatures cited above depend on variables such as cooling rate, diffusion domain size, and, for the (U-Th)/He system, accumulated radiation damage. Consequently, the approach adopted here explicitly accommodates these variables by integrating KfAr multi-diffusion domain modeling (Lovera and others, 1989; Lovera and others, 1997) with diffusional modeling of the lower temperature systems in order to develop continuous thermal histories from > 350°C to < 50°C (Zeitler, 1993; Ketcham, 2014; Zeitler, 2017). The continuous nature of the modeled cooling histories is also important better captures inflections in cooling rate.

Comparison with Northern REHW

In addition to integrating previously published results from Harrison Pass, these results can also be compared with new and previously reported thermochronology from the northern half of the REHW. The results from farther north record a three-phase exhumation history with the earliest phase occurring mostly during the Late Eocene but continuing into the early Oligocene (40 Ma to ~30 Ma), the second phase initiating in the late Oligocene (after ~26 Ma) or earliest Miocene and continuing to ~11 Ma, and the final phase corresponding to the Late Miocene to Recent Basin and Range extension.

The earliest phase of extension is recorded primarily by cooling of the Wood Hills and the southern East Humboldt Range through $^{40}Ar/^{39}Ar$ mica, ZFt, ZHe, AFT, and AHe closure (Dallmeyer and others, 1986; Dokka and others, 1986; McGrew and Snee, 1994; Wolfe and others, 2016; Wolfe and Rahl, 2016; Metcalf and others, 2018; Gonzalez and others, 2019; Jeruc and others, 2019; Metcalf and others, 2019; McGrew and others, 2019). For example, Wolfe and Rahl (2016) report ZHe dates ($T_c \approx$ 180°C) ranging from 37–40.5 Ma from the southeastern Wood Hills younging northwestward to 24–29 Ma in extensional mylonites underlying the detachment fault in the NW Wood Hills. Consequently, the high amphibolite facies rocks of the Wood Hills must have cooled to < 180°C by the late Oligocene, and extensional mylonitiztion must also have predated the late Oligocene.

Possibly the most compelling evidence for large magnitude Eocene extension comes from the southern East Humboldt Range where a dense sample transect underlying the detachment fault yields $^{40}Ar/^{39}Ar$ biotite, muscovite (MsAr), K-feldspar and ZHe ages that all record rapid cooling in the Late Eocene (mostly between 35 and 40 Ma) (McGrew and others, 2019; Jeruc and others, 2019). The detachment fault in this area juxtaposes a tilted sedimentary sequence of Pennsylvanian to Triassic rocks down against a regionally metamorphosed footwall sequence of Cambrian to Devonian strata, with the deeper parts of the section intruded by a suite of 10 m scale to 500 m scale peraluminous muscovite-garnet leucogranitic plugs dated at 84 Ma (Sample RM-12, Wright and Snoke, 1993). At the southern tip of the East Humboldt Range a Late Eocene volcanic sequence (39–41 Ma) (Brooks and others,1995) overlies the Triassic strata with angular unconformity, and appears itself to be cut and rotated by the detachment fault, although exposed field relationships do not definitively exclude the possibility that it may overlap the detachment. Therefore, the Late Eocene (~40 Ma) paleosurface was effectively faulted down against the metamorphosed core. In contrast to the sedimentary and volcanic sequence overlying the detachment fault, the metamorphosed lower plate rocks in this area include recently discovered kyanite-bearing schists correlative with the Dunderberg schist in the Wood Hills, where peak PT conditions of 610–630°C, 6.1–7.1 kb have been dated at 82.8 ± 1.1 Ma (Lu-Hf garnet) (Wills, 2014). Though thermobarometric investigation of the kyanite schist locality in the southern East Humboldt Range is still underway, PT conditions were likely comparable to those of the Wood Hills based on phase equilibria constraints. Even ignoring thermobarometric constraints, assuming simple restoration to inferred stratigraphic paleodepths would place these rocks above ZHe closure temperatures. Thus, there appears to be little recourse to explain the cooling and exhumation of these deep, mid-crustal rocks to upper crustal levels between 40 Ma and 35 Ma except by rapid, large-magnitude Late Eocene extensional exhumation on the overlying detachment fault.

Notably, this phase of extensional unroofing also corresponds with the principle extensional phase at Spruce Mountain, the inferred breakaway zone for the Late Eocene fault system (Pape and others, 2016). In addition, Canada and others (2020) infer a 42–43 Ma onset to extension regionally based on the sudden appearance of Late Eocene detrital zircon in the Elko Basin (mostly to the west of the REHW). We will henceforward refer to the inferred Late Eocene extension as the "Wood Hills phase" as its primary effect was to exhume most of the Wood Hills and southern East Humboldt Range.

In contrast, the later extensional phase in the northern half of the REHW appears to begin in the late Oligocene, and continues, possibly with episodic lulls, to ~10 Ma. It is recorded by WNW-directed cooling across the Ruby Mountains and central and northern East Humboldt Range (Dallmeyer and others, 1986; Dokka and others, 1986; McGrew and Snee, 1994; McGrew and others, 2019; Metcalf and others, 2018; Jeruc and others, 2019). The early stages of this phase of extension coincide with WNW-directed mylonitic shearing that overprints a variety of late Paleogene intrusive rocks (Wright and Snoke, 1993). However, cooling through $^{40}Ar/^{39}Ar$ mica closure by ~21 Ma implies that the mylonitic phase of extension was complete by the Early Miocene and that subsequent extension oc-

curred in the brittle upper crust. We will refer to this extensional episode as "REH phase extension." The final extensional episode post-dates ~10 Ma and includes the currently active normal faults bounding both flanks of the Ruby Mountains and East Humboldt Range, which we will refer to as "Basin and Range extension."

In contrast with the cooling and exhumation histories summarized above, the most comprehensive study of the cooling and exhumation of the southern part of the REHW reports little to no Late Eocene to Early Miocene extension (Colgan and others, 2010). Instead, Colgan and others (2010) interpret that the vast majority of the extension occurred after ~17 Ma, beginning synchronously with impingement of the Yellowstone hotspot in northwestern Nevada and active chiefly during the Middle Miocene. This interpretation is based primarily on low temperature AFT and AHe thermochronology from the Harrison Pass pluton. Although K-Ar and $^{40}Ar/^{39}Ar$ biotite ages show a westward-younging trend from the Late Eocene to the Early Miocene across the Harrison Pass pluton, Colgan and others (2010) do not interpret this trend as recording the progression of extensionally-driven unroofing, but rather attribute it to an eastward-tilted $^{40}Ar/^{39}Ar$ partial retention zone (PRZ) developed during conductive cooling of the Late Eocene stock. Additional support for this interpretation is provided by the observation that the Paleozoic stratigraphy of the country rock to the south of the pluton is tilted ~30–60° eastward, as well as by arguments developed by Burton (1997) that originally flat-lying sills in the pluton have also been tilted ~30° toward the East.

Problem and Approach

In addition to the absence of the Wood Hills phase extensional imprint, the Middle Miocene (17 Ma) onset for the REH phase of extension documented by Colgan and others (2010) significantly postdates the inferred Late Oligocene to Early Miocene extensional onset reported farther north (e.g., McGrew and others, 2019). Based on the ~17 Ma initiation of extension, Colgan and others (2010) infer that the approximately coincident impingement of North America over the Yellowstone hotspot was a key trigger mechanism for the onset of extension. Clearly, if the initiation of extension predated arrival of the Yellowstone thermal anomaly (as argued by McGrew and others, 2019), it could not have been caused by it. Consequently, there is a serious discrepancy between interpreted cooling and exhumation histories derived from the main part of the REHW farther north as contrasted with the southern part of the range centered on the Harrison Pass area. Resolving these conflicting interpretations is the chief purpose of this paper. To resolve this problem, below we complement the earlier reported low-temperature thermochronometry of Colgan and others (2010, and references therein) with new KfAr, TnHe and ZHe thermochronometry spanning the ~200°C temperature range between the BtAr and AFT systems. By integrating this data to develop diffusional models of continuous thermal histories from ~350–50°C, we seek to better resolve the onset and early evolution of extension in the Harrison Pass area as a basis for comparison with results from the higher grade part of the REHW farther north.

METHODS

Sampling and Geological Context

This study complements and supplements previously published low temperature thermochronometric data with newly collected KfAr, TnHe and ZHe results from the Harrison Pass pluton (Table 1). Sampling at intervals of 2–3.5 km defines a transect across the Harrison Pass pluton subparallel to the inferred tectonic transport direction for the REHW (approximately 300°). In order to compare sample ages in tectonic context, we have established a baseline along the western flank of the range (which we henceforward refer to as the "REHW baseline") (Figure 1). The REHW baseline also approximately coincides with the southeastern boundary of the "V-shaped" gravity high of northcentral Nevada as well as with the eastern limits of well-defined Neogene basin fill and the northwestern boundary of the REHW positive aeromagnetic anomaly (Ponce and others, 2011). Additional thermochronology is in progress to confirm and better delineate the results presented below.

Table 1. SAMPLE LOCATION INFORMATION.

Sample	Latitude[a]	Longitude	Elevation (meters)	Distance (km)[b]	Lithology/Systems Dated
RGD17-38	40.30997	–115.47489	1959	23.75	Granodiorite/ZHe
RGD17-39	40.31508	–115.49200	2038	22.4	Granodiorite/KfAr, TnHe, ZHe
RGD17-20	40.32619	–115.51047	2227	20.5	Granodiorite/TnHe
RGD17-21	40.32619	–115.51047	2227	20.5	Granodiorite/KfAr, ZHe
RGD17-19	40.32383	–115.55744	1998	17.2	Granodiorite/KfAr
RGD18-A6	40.34854	–115.5760	2022	14.2	Granodiorite/KfAr

[a]*All locations in decimal degrees, WGS84 datum.*
[b]*Distance in transport direction (decreasing toward the WNW) as measured from the REHW baseline (Figure 1).*

Analytical Methods

(U-Th)/He analyses were conducted at the University of Colorado Boulder TRaIL (Thermochronology Research and Instrumentation Laboratoty) whereas $^{40}Ar/^{39}Ar$ analyses were conducted at the University of Nevada—Las Vegas Nevada Isotope Geochronology Laboratory. After sampling as described above, pure mineral separations were obtained and samples were analyzed following methods detailed in Appendix 1.

Diffusion Modeling and Thermal Histories

Due to its moderate retentivity for argon over a broad temperature range from ~150–350°C, $^{40}Ar/^{39}Ar$ dating of potassium feldspar (K-feldspar) is a key thermochronometer linking higher and lower temperature systems (McDougall and Harrison, 1999). Low temperature plutonic K-feldspar such as those investigated here typically exhibit complex microstructures that commonly yield reliable thermal histories when modeled based on the assumption of multiple diffusion domain behavior (Lovera and others, 1989, 1991, 2002). In this approach, the step heating experiments described in Appendix 1 are used to independently constrain each sample's specific diffusion kinetics and domain size distribution. These data are then used to model thermal histories on geologic time scales that optimally fit the observed age spectrum. Since the results derive from laboratory-based diffusion experiments on the material being dated, the model results inherently incorporate the sample-specific diffusion domain structure and allow for the investigation of diverse cooling paths for comparison with the observed age spectrum. The model output is a continuous cooling history for each sample from ~350–150°C.

The thermal histories presented below were generated using the Arvert 6.1.1 code (Zeitler, 2017), a software package that allows the integration of KfAr multi-diffusion domain modeling as described above with explicit mineral constraints (e.g., BtAr ages) and with diffusion modeling of lower-temperature systems—e.g., the AHe, ZHe, and/or TnHe systems (Ketcham, 2014). Thus extended, Arvert can yield continuous thermal histories from > 350°C to < 70°C while optimizing internal consistency between a variety of thermochronometers. The inputs for this model are the observed age spectrum and the sample-specific diffusion models described in Appendix 1.

All samples investigated here showed the expected diffusive loss pattern required to appropriately model the KfAr system—i.e., after discounting excess argon in the lowest or highest temperature steps, the spectra show a step-wise release of ^{39}Ar that either remains age-consistent or (more typically) increases monotonically with increasing temperature (Figure 3). Modeling was conducted only over increments below the temperature of sample breakdown due to partial melting (~1100°C). We explored both infinite slab and spherical diffusion models, and here we present results from the model that generated the most reliable diffusion parameters as judged by comparison of the modeled with the observed $\log r - r_0$ domain size distributions and comparison of the activation energies and $\log (D_0 / r_0^2)$ values with those typically observed for basement potassium feldspar (Lovera, and others, 1997). Due to the nature of the ^{39}Ar release, just one sample (RGD17-39) failed to yield a good fit based on the automatically generated regression of the three lowest temperature steps. For this sample, we chose an alternative domain model based on an unweighted regression on steps 3–6 that fell within the expected range of values reported by Lovera and others (1997) (Figure 3).

It is important to understand that Arvert utilizes a controlled random search algorithm to generate a family of optimal solutions for the thermal history using the mean square of weighted deviates (MSWD) as the objective measure of fit between the modeled and observed spectra and other specified mineral constraints. Thus, it does not return a statistically determined confidence level envelope, but rather yields a range of acceptable-fit solutions, with the "best-fit" solutions within that range indicated in green and the "worst-fit" in red (Figure 3). Paths that were tried but discarded are shown in pale gray. Because Arvert seeks the best-fit solution, the relative width of the band of best-fit solutions tends to narrow the longer the program runs. Accordingly, it may overstate uncertainties (and, more importantly, fail to "discover" the best-fit solution) for too few trials whereas it tends to over-converge on the best-fit solution for more extended runs—possibly discarding paths that may be within a reasonable uncertainty envelope of the "best-fit" solutions. Nevertheless, the width of the band is meaningful in that it suggests how strongly constrained the overall path is, and which aspects of the cooling history are most strongly constrained.

Since all samples were from the Harrison Pass pluton, we specified starting conditions of 550–750°C at 40 Ma. We were unable to specify the 36 Ma age of the pluton as the "start time" because Arvert requires a minimum modeled run time before the system begins to close. Therefore, the part of the returned histories above ~350°C are mostly constrained by the user-specified start time and temperature, and similarly the lowest part of the thermal history (below ~50°C, assuming the AHe system is included in the mineral constraints) is mostly constrained by the requirement that the sample end the run at the estimated mean surface temperature. We typically explored a minimum of ten model runs systematically varying the explicit time-temperature constraints, whether or not heating was allowed in the thermal history, and alternately including or ignoring constraints from adjacent thermochronometers (i.e., the AHe, ZHe, TnHe, or BtAr systems). This yielded a good understanding of what parts of the thermal history were most robust regardless of the constraints specified versus those parts of the thermal history that were more sensitive to variations in specified constraints. For display in Figure 3, we chose model runs that incorporated the maximum number of mineral constraints available while still yielding a good fit as judged by the MSWD for the run. All four samples yielded reasonably robust results that were not over-sensitive to input assumptions.

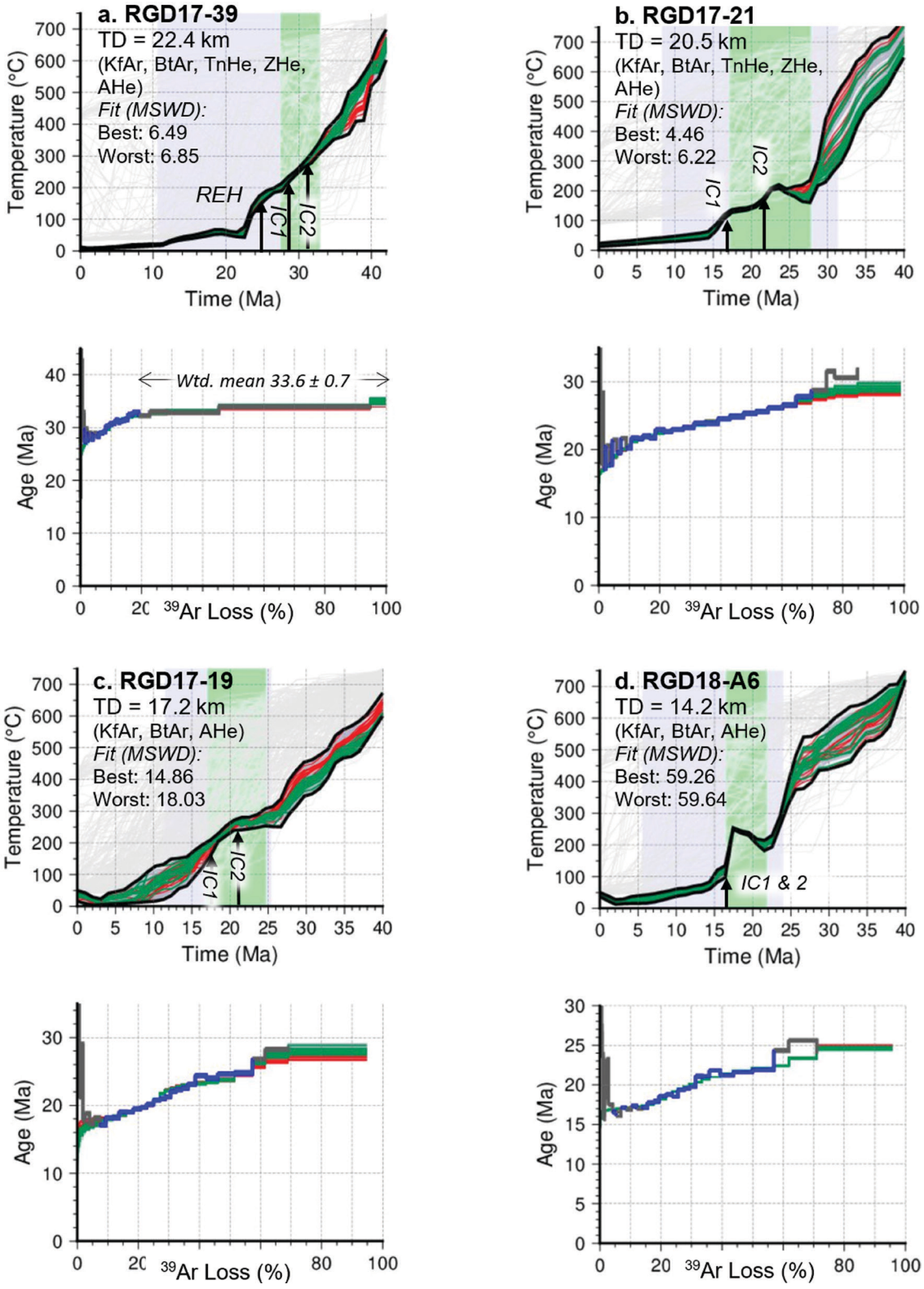

Figure 3. Thermal histories modeled with Arvert for samples (a) RGD17-39, (b) RGD17-21, (c) RGD17-19, and (d) RGD18-A6. Top row presents best-fit thermal models with systems included and arrows indicating the ages of corresponding bounding isochrons (compare Table 3). An ensemble of histories with acceptable fits are shown with Best fit histories indicated in green and worst fit in red. The pale green shaded region indicates the range of the KfAr spectrum, and the pale gray "spaghetti lines" indicate all trial paths. Second row presents modeled age spectra (in green and red, as described above) compared with the observed spectrum (blue). Model parameters are provided in Appendix 3.

Finally, as a consistency check on the modeled thermal histories, we also generated bounding isochrons on the inverse isochron plot using IsoplotR (Vermeesch, 2018). These samples typically yielded linear arrays over the lower temperature steps (excluding steps with conspicuous extraneous argon) that contrasted in age and/or $^{40}Ar/^{39}Ar_i$ ratios with isochrons based on the intermediate to higher temperature steps. In some cases, the inverse isochron ages correlated with distinct inflections in the thermal histories, enhancing our confidence in the significance of both results (Figure 3).

RESULTS

The thermochronologic constraints developed here are presented in Tables 2 and 3, Figures 3 and 4, and Appendix Tables A1 and A2. Sample locality information is summarized in Table 1 whereas Table 2 summarizes the (U-Th)/He results and Table 3 summarizes the KfAr results. The samples form a transect through the Harrison Pass pluton approximately parallel to tectonic transport direction, with distances decreasing toward the WNW. Figure 4 plots observed ages versus distance parallel to the tectonic transport direction.

The KfAr spectra show extraneous argon release in the lower temperature steps, which was adequately treated by the standard practice of running duplicate isothermal steps. Overall, the spectra show well-behaved step-release patterns that were appropriate for multi-diffusion domain modeling. For comparison with the multi-diffusion domain model results, upper and lower bounding isochrons were defined for each of the KfAr samples (Table 3). All isochrons reveal the same WNW-younging pattern evident in the age spectra and in the other thermochronometric systems, as would be expected in either the rotated PRZ or the extensionally-driven cooling models discussed in detail below.

For the farthest east sample (RGD17-38 at a distance of 23.75 km up-dip from the REHW baseline) three zircon aliquots range in age from 19.75 ± 0.52 Ma to 24.72 ± 0.47 Ma suggesting cooling in the early Miocene (Table 2). Slightly farther to the WNW, sample RGD17-39 (22.4 km up-dip from the REHW baseline) also yields evidence of early Miocene to late Oligocene cooling. Three TnHe ages range from 22.66 ± 0.47 to 28.97 ± 0.99 Ma and six ZHe aliquots range in age from 19.32 ± 0.79 to 24.96 ± 1.24 Ma (Table 2).

In addition to the above (U-Th)/He results, sample RGD17-39 also yields a KfAr age spectrum showing step release from a quasi-plateau in the upper temperature steps with a weighted mean age of 33.6 ± 0.7 Ma. A bounding isochron on the upper temperature steps indicates an age of 30.7 ± 0.5 Ma whereas a bounding isochron calculated on the lower temperature steps yields an age of 28.4 ± 0.4 Ma (confidence intervals on isochrons include dispersion as described by Vermeesch, 2018).

Probably because so much of the ^{39}Ar was released in the highest temperature steps, KfAr sample RGD17-39 was the only sample that did not yield a well-constrained domain model. Nevertheless, a regression of the diffusion parameters on steps 3–6 of the release yields a well-constrained and reasonable thermal history that integrates tightly with the above summarized TnHe and ZHe data, as well as with nearby BtAr and AHe results previously reported by Colgan and others (2010) (Figure 3a). Within 600 m of RGD17-39, Colgan and others (2010) report AFT ages of 16.3 ± 1.5 Ma and 15.1 ± 1.6 Ma and AHe dates of 16.7 ± 1.1 Ma and 16.5 ± 2.8 Ma from their samples JC05-HP8 and HP9, respectively. In addition, they report a BtAr age of 34.31 ± 0.06 Ma from their sample JC05-HP9. Diffusive modeling incorporating all of the above mineral constraints was integrated with Kfs multi-diffusion domain modeling using Arvert 6.1.1, yielding a well-constrained thermal history for the upper part of the pluton (Figure 3a). The initial rapid cooling phase inferred from the isochron and weighted mean ages is also evident in the modeled cooling history, which yields a steep, concave-upward profile with cooling rates in excess of 25°C/m.y. Though it would be difficult to definitively exclude a component of early extension-related cooling, this result is consistent with relaxation of the upper crustal geotherm following a thermal event associated with emplacement of the Harrison Pass pluton into the upper crust. The cooling history appears to approach an asymptote at ~180°C by ~25 Ma, after which there is an inflection to steeper cooling rates in the latest Oligocene to earliest Miocene that we interpret below as marking the initiation of REH-phase extension.

At a transport direction distance of 20.5 km, sample RGD17-21 represents the central part of the pluton. It yields a KfAr spectrum showing step release from ~28 Ma to < 17 Ma, with two bounding isochrons, one on the higher temperature steps at 21.8 ± 0.7 Ma and another on the lower temperature steps at 16.8 ± 0.5 Ma (Table 3). Additional constraints are provided by two ZHe ages of 20.01 ± 0.64 and 16.05 ± 0.33, respectively, and an adjacent sample (RGD17-20) that yielded three TnHe ages ranging from 19.75–24.72 (Table 2). In addition, Colgan and others (2010) report a BtAr age of 31.35 ± 0.06 Ma, an AFT age of 16.2 ± 1.3, and an AHe mean age of 13.4 ± 0.4 from their sample H05-RM104 collected approximately 500 m from samples RGD17-20 & 21. These data were also included in the thermal history shown in Figure 3, although multiple runs were conducted including or excluding these mineral ages to test for consistency of results. As elaborated in the Discussion below, accelerations in the modeled cooling history at ~23 Ma and ~17 Ma, suggest the possibility that the isochron ages approximate the timing of two sub-pulses in the Miocene cooling and unroofing history (Table 2).

Sample RGD17-19 (17.2 km up-dip) shows a step-release spectrum resembling that of sample RGD17-21 above, with an isochron age of 21.0 ± 0.4 Ma on the upper temperature steps, and 17.5 ± 0.4 Ma on the lower temperature steps. In this case, we do not yet have ZHe or TnHe results, but Colgan and others (2010) report a BtAr age of 25.40 ± 0.07 Ma, an AFT age of 16.4 ± 2.4 Ma, and an AHe age of 17.0 ± 1.0 Ma from their sample JC05-HP4 collected approximately 120 m away. We note that the corrected AHe age is older than both the co-located AFT

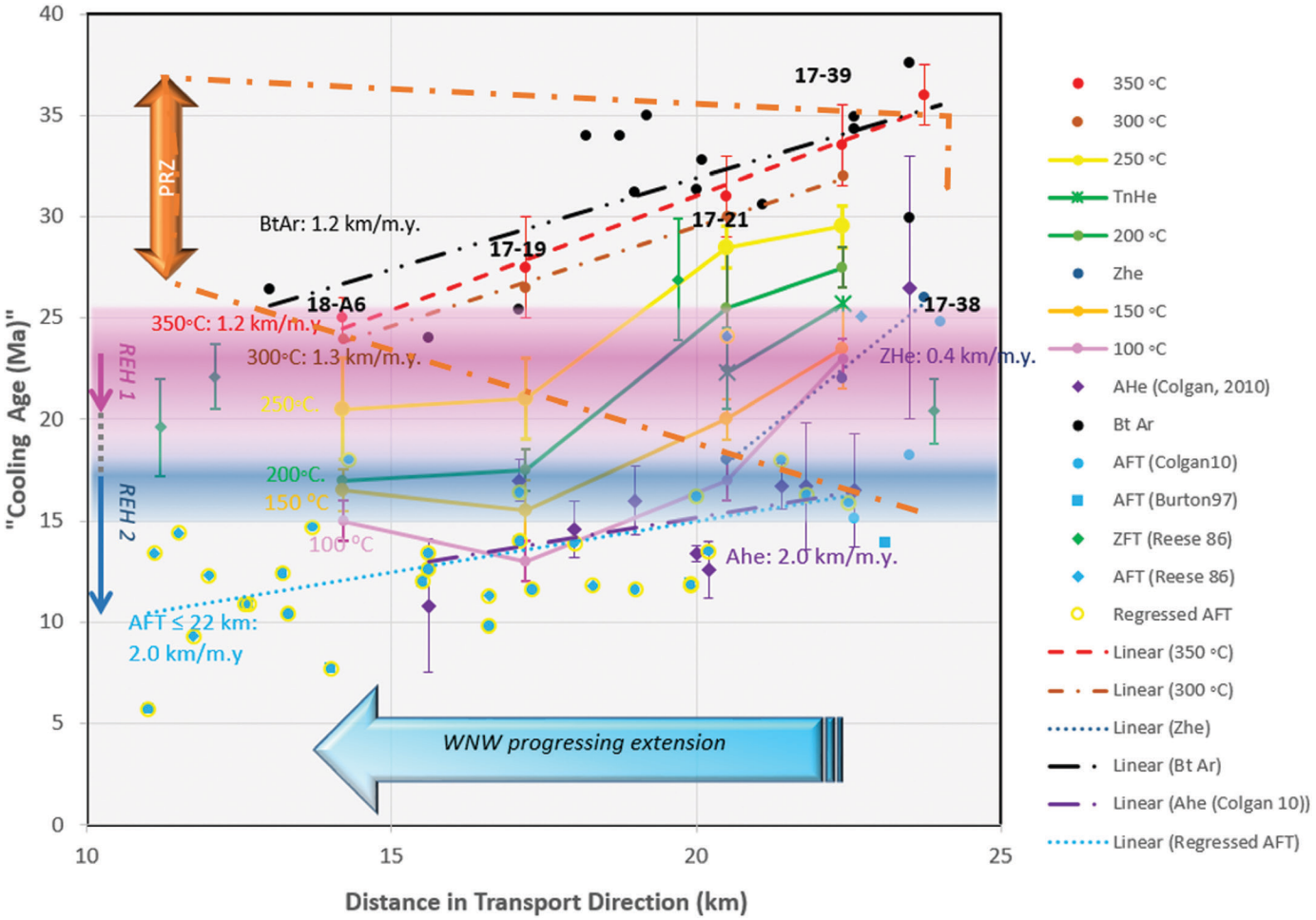

Figure 4. Time-distance diagram illustrating variation in cooling ages with distance in transport direction as measured from a base line along the west flank of the REHW (See Figure 1). Isotherms are defined by the time of cooling through benchmark temperatures in the cooling histories presented in Figure 3. Also shown are the apparent cooling ages for the BtAr, TnHe, ZFT, ZHe, AFT, and AHe systems synthesizing results from this study with previously published data (Kistler and others, 1981; Reese, 1986; Burton, 1997; Colgan and others, 2010). The rose-colored, gradient-shaded band indicates the range of possible starting times for REH-1 phase extension in the Harrison Pass region, with the most likely times of initiation indicated by darker shading and less likely times in lighter shading. The gradient-shaded blue band similarly indicates the probable age of onset of REH-2 extension. Linear best-fit trendlines are provided for systems that appear to show linear relationships whereas systems that appear to show possible inflections are merely connected by lines. Note the possibility of a brief lull in extension between ~20 and ~17.5 Ma. The WNW-directed progression of cooling ages is recorded in all systems; the orange double-headed arrow and associated dot-dash line indicate the likely range of partial retention (or partially annealed) ages.

age and the regional age trend. The best-fit cooling history, like that of RGD17-21, flattens at ~25 Ma before reaccelerating at ~21 Ma (approximately synchronous with the isochron on the higher temperature steps). Unlike RGD17-21, sample RGD17-19 does not preserve evidence of a second inflection at ~17 Ma, but the near correspondence of the lower temperature KfAr bounding isochron (17.5 Ma) with the AFT age (16.4 Ma) and the AHe age (17.0 Ma) suggests rapid cooling after ~17.5 Ma.

Finally, from the farthest west and deepest structural levels of the pluton, sample RGD18-A6 (14.2 km up-dip) exhibits a step-release KfAr age spectrum from ~25 Ma to ~16 Ma and bounding isochrons over the higher and lower temperature steps yielding statistically identical ages of 16.4 ± 0.6 and 16.4 ± 1.1 Ma, respectively. The closest results reported by Colgan and others (2010) are their samples JC05-HP2 and HP3, 1.75 and 2.0 km to the south, respectively. However, with up-dip distances of 13.7 km and 15.6 km, respectively, these samples bracket the position of Sample RGD18-A6. They report an AFT age of 14.7 ± 1.6 Ma from sample JC05-HP2 and from sample HP3 a BtAr age of 24.03 ± 0.06 Ma, an AFT age of 13.4 ± 2.0 Ma, and an AHe date of 10.8 ± 3.3 Ma (Colgan and others, 2010).

Given the distance of the above BtAr and AHe results from sample locality RGD18-A6, the thermal history of RGD18-A6 was tried both with and without the additional mineral constraints provided by the BtAr and AHe results reported by Col-

Table 2. (U-Th)/He ZIRCON AND TITANITE AGE DATA.

Full Sample Name	Distance (km)a	Length 1 (mm)	Width 1 (mm)	Width 2 (mm)	Dim Mass (mg)	r_s (mm)	4He (nmol/g)	±	U (ppm)	±	Th (ppm)	±	Sm (ppm)	±	Uncorrected Date (Ma)	Ft	Corrected Date (Ma)	Analytic Uncertainty (Ma; 2σ)
RGD17-38_z01	23.75	283.1	119.5	115.5	13.0	72.4	36.3	0.1	261.2	8.6	120.2	39.9	1.0	0.3	23.24	0.841	27.62	2.42
RGD17-38_z04		397.9	154.0	175.0	36.1	101.3	650.7	1.7	5480.1	75.1	539.2	4.8	1.3	0.1	21.50	0.886	24.25	0.64
RGD17-38_z05		319.4	135.4	111.2	16.5	76.6	199.2	0.8	1462.2	17.0	408.1	8.8	3.1	0.2	23.67	0.850	27.83	0.64
RGD17-39_t01	22.4	391.9	343.5	120.0	40.7	97.4	32.0	0.1	166.9	4.2	296.3	4.0	10.4	0.1	24.97	0.862	28.97	0.99
RGD17-39_t02		314.0	229.4	98.3	14.0	73.3	30.5	0.1	240.6	2.9	267.9	5.0	29.0	0.4	18.59	0.820	22.66	0.47
RGD17-39_t03		275.7	203.1	72.4	7.5	54.2	36.2	0.1	270.9	5.3	333.8	2.7	47.7	0.7	19.15	0.758	25.26	0.68
RGD17-39_z01	22.4	274.6	98.2	100.7	9.7	63.4	155.6	0.9	1685.0	77.3	237.4	51.7	36.5	61.1	16.57	0.821	20.17	1.46
RGD17-39_z02		237.2	84.6	81.8	5.8	53.2	139.2	0.9	1234.8	41.6	325.1	12.1	0.5	0.5	19.67	0.788	24.96	1.24
RGD17-39_z03		185.9	87.2	79.0	4.2	50.3	85.3	0.4	1019.9	37.1	287.5	11.1	0.0	0.6	14.54	0.776	18.73	0.97
RGD17-39_z04		262.0	110.6	99.4	9.7	65.0	82.2	0.3	902.8	19.5	224.8	11.8	1.2	0.4	15.95	0.825	19.32	0.79
RGD17-39_z05		313.9	102.7	98.1	11.7	65.4	214.1	0.8	2075.6	38.5	418.6	4.7	0.7	0.1	18.25	0.826	22.08	0.78
RGD17-39_z06		295.5	103.5	105.6	11.6	67.0	70.7	0.2	633.4	10.5	227.0	2.7	0.9	0.2	19.07	0.829	22.99	0.70
RGD17-20_t01	20.5	547.7	329.6	169.5	70.2	131.0	21.2	0.1	172.6	2.6	205.1	5.7	6.1	0.0	17.73	0.898	19.75	0.52
RGD17-20_t02		542.1	482.6	192.0	128.5	150.2	18.3	0.1	117.9	1.6	197.2	5.9	3.3	0.0	20.64	0.910	22.69	0.57
RGD17-20_t03		656.1	463.1	103.2	43.6	66.4	52.0	0.2	378.6	4.6	461.6	11.3	9.8	0.1	19.73	0.798	24.72	0.47
RGD17-21_z02	20.5	532.1	119.5	105.5	26.8	77.0	73.9	0.2	747.4	13.1	242.8	2.2	0.5	0.0	17.03	0.851	20.01	0.64
RGD17-21_z03		404.0	118.6	112.1	20.0	76.3	32.0	0.1	406.1	4.3	124.4	1.7	0.5	0.1	13.64	0.849	16.05	0.33

[a]*Distances measured up-dip from the REHW baseline (see Table 1 and description in text).*

gan and others (2010). The timing of inflections in the cooling history did not vary significantly whether or not the AHe and BtAr results were included, and the fit to the data with inclusion was significantly better, so the thermal model reported in Figure 3d includes the AHe and BtAr mineral constraints from Colgan and others (2010). Notably, the early Miocene cooling history recorded by the samples from shallower structural levels does not appear to be preserved in the western part of the pluton, being recorded only by the upper part of the KfAr age spectrum and the 24-Ma BtAr age reported by Colgan and others (2010). In addition, the best fit of the KfAr MDD model converged on a solution with a heating event from ~200 to ~250°C starting after 22 Ma and reaching a sharp peak at 17.5 Ma before suddenly dropping > 100°C in 1 m.y. (Figure 3d). Final cooling through AFT and AHe closure appears to have proceeded more gradually thereafter. However, we have not yet obtained ZHe and TnHe results from this locality to incorporate into the thermal model and enhance our confidence in this result.

Figure 4 summarizes the above cooling histories against distance parallel to tectonic transport direction as determined from the REHW grid (Figure 1). For the thermal history models it maps the approximate time of passage through benchmark isotherms 350°C, 300°C, 250°C, 200°C, 150°C, and 100°C; for other thermochronometric systems the cooling histories are plotted using nominal closure temperatures of the systems. It should be noted that the "error bars" on these systems represent analytical uncertainties only for the AFT and AHe systems. For the other systems they represent the range in ages observed (TnHe, ZHe) or the range in observed "best-fit" ages at a given temperature for the thermal models. The colored bands and double arrows decorating the diagram indicate our preferred interpretation of the cause and timing of cooling events and will be discussed in detail below. The chief trend evident in this diagram is that all thermochronometric systems show a distinct age gradient younging westward. The highest temperature systems ($T_c \geq 300$°C) show an apparent age gradient of ~1.2 Ma/km whereas the lowest temperature systems (AFT and AHe) show age gradients of ~2.2 Ma/km; intermediate systems show "kinked" cooling profiles, with higher temperature and farther up-dip systems tending to follow the older age trends of the higher T_c systems whereas the lower temperature or farther down-dip systems tend to follow the younger age trends of the AFT and AHe systems.

DISCUSSION

Interpretation of the extensional history of the Harrison Pass area is complicated by the the interactions between extensional history and the thermal evolution of the crust. As illustrated in Figure 4, the general picture is clear: every thermochronometer investigated reveals westward-younging ages consistent with exhumation beneath a westward-dipping normal fault system beginning no later than ~17 Ma, broadly consistent with the previous interpretations of Colgan and others (2010). However, understanding the precise timing and progression of extensional initiation hinges critically on understanding the thermochronologic record in the context of the broader geologic setting.

The chief goal of this investigation is to constrain the timing of onset of extension in the Harrison Pass area. A key question is whether the early Oligocene BtAr dates from the eastern part of the Harrison Pass pluton record cooling driven at least in part by extensional unroofing, or whether they instead represent a rotated PRZ as argued by Colgan and others (2010). If extension in the Harrison Pass area did not begin (or at least was not significant) before the mid-Oligocene, when did it begin? Specifically, did it begin in the mid- to late Oligocene, concurrent with the timing of the second major phase of extension reported from the northern REHW, or did it initiate after ~17.5 Ma as inferred by Colgan and others (2010)? The following sections address these questions in chronological order.

Late Eocene to early Oligocene Cooling history

The data presented in Tables 1–3 and Figures 3 and 4 clearly record rapid early Oligocene cooling at intermediate to high temperatures from the structurally higher eastern half of the Harrison Pass pluton. The farthest east and structurally highest sample, RGD17-38 (Table 2, Figure 4) cooled from pluton emplacement temperatures of >700°C through BtAr closure ($T_c \approx$

Table 3. $^{40}Ar/^{39}Ar$ POTASSIUM FELDSPAR ISOCHRON DATA.

		Isochron 1 (low temperature steps)						Isochron 2 (high temperature steps)					
Sample	Distance[4] (km)	Steps Included	Age (Ma)	±[5]	$^{40}Ar/^{36}Ar_i$	±[b]	MSWD	Steps Included	Age (Ma)	±[b]	$^{40}Ar/^{36}Ar_i$	±[b]	MSWD
RGD17-39	22.4	4, 6, 8, 10–18	28.4	0.4	363	37	42	19–32	30.7	0.5	459	46	100
RGD17-21	20.5	2, 4, 6, 8	16.8	0.5	350.3	4.2	1.3	15–34	21.8	0.7	750	97	580
RGD17-19	17.2	4, 6, 8-13	17.5	0.4	354	14	110	20–26	21.0	0.4	463	35	32
RGD18A-6	14.2	1, 3-5, 7, 9, 11–18	16.4	0.6	360	18	200	20–31	16.4	1.1	696	74	65

[4]Distance in transport direction (decreasing toward the WNW) as measured from the REHW baseline (Figure 1).
[5]Uncertainties presented as confidence interval including dispersion as calculated by IsoplotR (Vermeesch, 2019).

325°C) by 30 Ma and through ZHe closure ($T_c \approx 180$°C) by ~25 Ma—a cooling rate decelerating over time from > 60°C/m.y to < 30°C/m.y. The more fully constrained result from the cooling model presented in Figure 3A (sample RGD17-39) (see also Tables 2 and 3 and Figure 4) requires a similar, though slightly younger cooling history.

The rapid early Oligocene cooling history can be attributed alternatively to extensional unroofing or to conductive cooling of the pluton followed by longer-term thermal relaxation of the crust following the widespread Late Eocene magmatic episode. Evaluating these alternatives depends on a variety of unknowns, not all of which are constrained in the Harrison Pass area. Among these are rate of conductive cooling, the possibility of convective contributions to the cooling history, whether the regional geothermal gradient is increasing or decreasing, and (if extension is involved) the rate, magnitude and mechanism of extension (e.g., Whittington and others, 2009; Murray and others, 2018; Zuza and others, 2019).

The most important constraint in the case of the Harrison Pass pluton is the structural reconstruction of the depth of pluton emplacement. As discussed in the Geologic Setting section above, the Harrison Pass pluton was probably emplaced at the approximate stratigraphic depths of the country rocks that it intrudes. The inferred roof of the pluton at its eastern contact intrudes the lower Pogonip Group at an inferred stratigraphic depth of ~4–6 km (Colgan and others, 2010). Figure 5 presents a simplified conceptual framework that illustrates how the observed cooling histories could be achieved simply by a Late Eocene heating event associated with pluton emplacement followed by thermal relaxation to a more stable geotherm of ~30°C/km similar to that of the modern Basin and Range province (e.g., Blackwell, 1983). The initial geotherm for this model (Figure 5c) is based on an assumed emplacement temperature of at least 650°C at the roof of the pluton. Although the regional geotherm during the Late Eocene is poorly constrained, widespread Late Eocene to early Oligocene volcanism across northern Nevada and deep-seated magmatism in the REHW support the inference that the geothermal gradient was probably high (e.g., Wright and Snoke, 1993; Brooks and others, 1995; Henry and John, 2013). In addition, thermobarometric estimates on the conditions of Paleogene extensional mylonitization from the northern REHW also imply an elevated geotherm—potentially even higher than the 40°C/km geotherm assumed here (e.g., Hurlow and others, 1991; Hodges and others, 1992). Consequently, the subsequent period (the Oligocene) was likely a time of thermal relaxation and crustal re-equilibration to a lower geothermal gradient.

In light of the above constraints, if Late Eocene extension did accompany pluton emplacement, its thermal signature could be difficult to deconvolve from simple thermal relaxation of the crustal geotherm. Given the relatively shallow emplacement depth of the pluton (~4–6 km in the east to ~11–12 km in the NW), even a small amount of extension would likely have cooled the shallow eastern part of the pluton through closure of the lower temperature thermochronometers. Consequently, the observation that the pluton did not cool through closure of the AFT and AHe thermochronometers until the Miocene severely limits the magnitude of any possible Late Eocene or early Oligocene extension. Figure 6 illustrates the effect that the first increments of extension would likely have had on the cooling histories from different structural levels in the pluton. Though the primary purpose of this figure is to illustrate our interpretation of latest Oligocene to early Miocene extension (see below), it also serves to illustrate the constraints on the possible magnitude of Late Eocene extension.

Clearly, there are many uncertainties here—e.g., the dip of the fault, the precise position of the "breakaway zone," the geothermal gradient, and the kinematics of isostatic response. For example, a steeper fault would result in a steeper uplift path with more cooling for a given amount of extension. In addition, the model presented in Figure 6 approximates a flexural response to accommodate isostatic uplift. Alternatively, accommodating the isostatic uplift of the lower plate by vertical simple shear would approximately double the rate of vertical exhumation (and thus the inferred cooling rate) for a given increment of horizontal extension. To investigate the sensitivity of the cooling history to some of these variables, the table beneath the cross-section presents cooling histories for a range of reconstructed paleodepths of each of the samples reported above, and for a variety of possible geothermal gradients from 25–40°C/km. Thus, the reported temperature ranges at each sample locality at 25 Ma (third column from left) can be compared with the estimated temperatures at any given paleodepth for a particular geothermal gradient.

The most comparable model temperatures to the 25 Ma temperatures are highlighted in cyan in the table underlying the cross-section. Only by maintaining a relatively high geothermal gradient of 30–40°C/km throughout the Oligocene would it be possible to match the observed cooling histories following 4 km of latest Eocene to early Oligocene extension. While possible, we view this as an upper limit on the plausible magnitudes of Late Eocene to early Oligocene extension near Harrison Pass. However, we agree with Colgan and others (2010) that little to no extension is required before the late Oligocene, and the analysis of subsequent extensional phases adopts the simplest assumption that there was no Late Eocene extension.

REH-Phase Extensional Onset

The most difficult issue is the timing of initiation of the REH phase of extension. The newly acquired data at least raise a question as to whether it may have begun earlier than the ~17 Ma start date inferred by Colgan and others (2010). As discussed above the BtAr system has a high enough closure temperature that most BtAr ages are likely partial retention ages as surmised by Colgan and others (2010). Assuming cooling to an ambient geothermal gradient resembling that of the modern northern Basin and Range province (29 ± 5°C/km), only the northwestern part of the pluton would likely have been near or

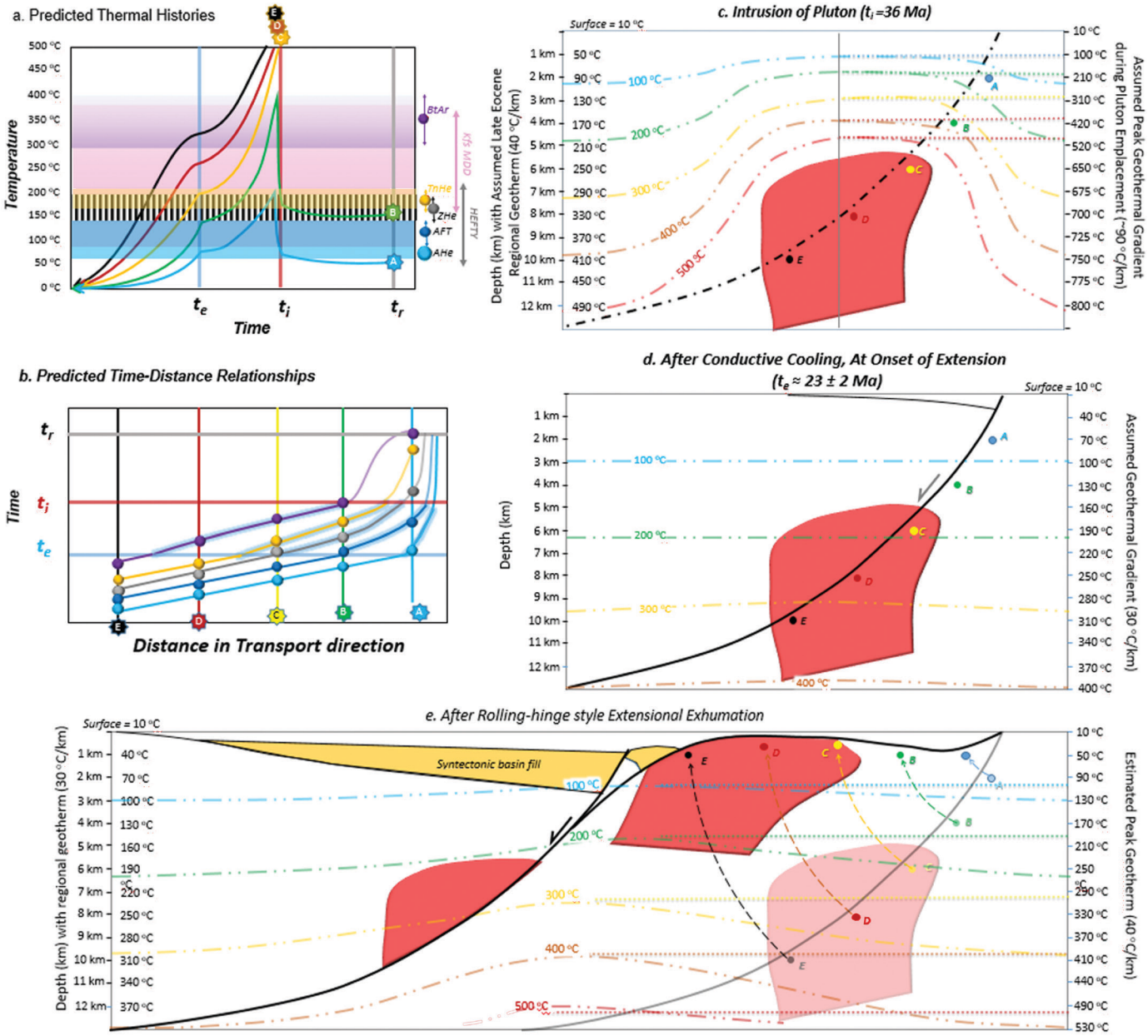

Figure 5. Conceptual cartoon illustrating expected cooling age patterns resulting from rolling hinge-style exhumation of the lower plate of a metamorphic core complex. (a) Predicted thermal histories for points A–E at regularly spaced intervals in the lower plate of the fault depicted in cross-sections c, d, and e. Closure temperature bands for the various thermochronometers pertinent to this investigation are illustrated on right side of diagram. (b) Predicted time-distance relationships for the thermochronometers introduced in (a). (c) Hypothesized temperature field surrounding pluton immediately following emplacement. (d) Same as in (c) but after conductive cooling of pluton and relaxation of regionally elevated geothermal gradient and immediately before the onset of extension. (e) State of the crust after ~16 km extension.

above the nominal BtAr closure temperature of ~325°C before the onset of extension.

As shown in Figure 5, the timing of onset of extension would ideally be marked by temporally coincident inflections in the cooling histories at any given point along the transect (Figure 5a) and/or by geographically defined inflections on the time-distance plots (Compare Figures 5b, d and e). However, if as illustrated in Figure 5b extension initiated in a crustal section that was already cooling, the expected inflections in cooling rates on the time-distance graphs could be subtle or imperceptible and the most pronounced inflections could even predate the onset of extension. The expected inflection in cooling rates in the thermal histories at the onset of extension on the time-temperature graphs (Figure 5a) appears more likely to be reli-

able, but here, too, the inflections may be suppressed for some thermochronometric systems if imposed on an already cooling crustal section.

Conversely, if the geographic inflection points in the AHe and AFT cooling histories are not preserved (e.g., either by erosion, non-sampling, or, as may be the case here, due to cross-cutting younger faults), then these systems may underestimate the timing of extensional onset (Figure 5b). By connecting the moderate with the low temperature thermal histories in order to model continuous thermal histories for the TnHe, ZHe and KfAr systems we gain crucial leverage in addressing these problems. Figures 3 (compare to Figure 5a) and 4 (compare to Figure 5b) do, in fact, show the anticipated inflections, but especially in Figure 4 they are not perfectly contemporaneous but rather are time-transgressive between approximately 25 Ma and 17.5 Ma. Below, we argue that this "smearing" of results could be explained by nonlinearities in both the rate of extension and/or the thermal evolution of the system during the early phases of extension.

We begin by considering the time-temperature histories (Figure 3). As discussed in the Results section above, it is important to recognize that the cooling histories above the green bands in the thermal history models are mostly constrained by the time and temperature of pluton emplacement. With this limitation in mind, comparing the results in Figure 3 with Figure 4a suggests that sample RGD18-A6 from the deepest structural levels in the western part of the pluton chiefly records only the post-18 Ma component of the cooling history. However, the ~24-Ma BtAr ages reported by Colgan and others (2010) from the western part of the pluton are nearly time-coincident with the early steep cooling histories recorded by the KfAr diffusion models from the same area, suggesting that they may record a latest Oligocene onset of extensional exhumation and rapid cooling (Figures 3c, 3d, and Figure 4).

Samples from higher structural levels build a more compelling case for a late Oligocene initiation of extension, with each showing inflections to faster cooling trajectories in the 21–24 Ma time window, which is our preferred timing for the initiation of extension. Particularly compelling is sample RGD17-39, which shows a sharp acceleration in cooling rate at ~25 Ma resulting in cooling to < 100°C by 21 Ma (Figure 3a). This abrupt acceleration in cooling rate also agrees well with a nearby AFT result of 24.1 ± 5.2 Ma reported by Reese (1986). With an estimated pre-extensional paleodepth of 6.5 km (Figure 6), cooling of this magnitude would be difficult to explain without significant extension. This timing is also consilient with results from samples RGD17-19 and 17-21 from deeper structural levels, both of which show Early Miocene KfAr inverse isochron ages (IC2, Table 2) with correlative inflections in the cooling curves (Figures 4b and 4c).

However, the cooling histories in Figures 3b and 3d suggest a lull in cooling after this initial cooling event, followed by a re-acceleration in the cooling histories after ~17.5 Ma. This renewed acceleration in the cooling histories is recorded by bounding isochrons defined over the lowest temperature steps in the KfAr spectra for samples RGD17-19 and 17-21, and RGD18-A6. In addition, these cooling events correspond well with the proposed initiation of rapid cooling reported by Colgan and others (2010). We suggest that these histories most likely record a two-step initiation to the extensional history, with an abortive initiation to extension between ~25 Ma and 21 Ma followed by a lull and then a renewal of rapid extension and exhumation after ~17.5 Ma.

This interpretation can be evaluated further in light of the time-distance relationships illustrated in Figure 4, which can be compared to the predictions in Figure 5b. Figure 4 graphs the approximate time of closure for the various isotope systems against distance in the inferred transport direction. For the integrated cooling history models (Figure 3) it records the timing of passage through benchmark isotherms 350°C, 300°C, 250°C, 200°C, 150°C, and 100°C, respectively. It should be noted that the "error bars" on these systems represent uncertainty envelopes only for the AFT and AHe systems. For the ZHe and TnHe systems they represent the range in ages observed, and for the integrated cooling history models, the error bars represent the range in observed "best-fit" ages at a given temperature. The rose-colored band across the middle of Figure 5 indicates the timing of the early extensional and cooling phase inferred above (23 ± 2 Ma), which we will term "REH 1," whereas the paler hues denote the proposed extensional lull between ~20 and ~17.5 Ma; and the blue shading indicates the most likely timing of reaccelerated extension post-dating 17.5 Ma ("REH 2").

As expected, all systems in Figure 4 show WNW-younging age trends, but the rate of younging varies, and the sampling density is insufficient to precisely define the position of major inflections, although such inflections are evident. The time-temperature curves for the intermediate closure temperature systems all appear to show distinctly steeper trajectories in the eastern half of the pluton (i.e., ZHe, TnHe, and the 150°C to 250°C isotherms) (Figure 4). Before ~25 Ma (labeled "PRZ" in Figure 4), we interpret cooling age trends to record partial retention of ^{40}Ar following pluton emplacement. Consequently, these should be considered "apparent cooling ages." A tighter sampling density would be ideal to capture the nuances of these variations, but the results are suggestive nonetheless.

We interpret the BtAr cooling ages and the 350°C and 300°C isotherms to be entirely or almost entirely within the PRZ, except perhaps for the westernmost samples, as noted above. Accordingly, the apparent WNW-younging age gradient within the PRZ probably reflects the mixed effects of the downward relaxation of isotherms following pluton emplacement and the thickness of the PRZ—i.e., these would be mixing ages of indeterminant geologic significance. However, the similarity of BtAr ages and the early parts of the KfAr cooling histories from the western part of the pluton with the ZHe and TnHe ages from the east, suggests that the westernmost sample (RGD18-A6) may have been at or near the base of the partial retention

Key Assumptions

1) 4 km extension
2) Fault daylights at ~30 km up-dip distance
3) Original Listric Fault geometry modeled after Wells Earthquake fault.
4) Geotherm of 27.5 °C/km; surface temperature 10 °C.
5) Room problems accommodated in part by HW collapse on antithetic shear planes yielding ~1 km vertical relief.
6) Remainder of room problem accommodated by isostatic flexural uplift of lower plate approximated along circular arcs hinged about breakaway zone of fault.

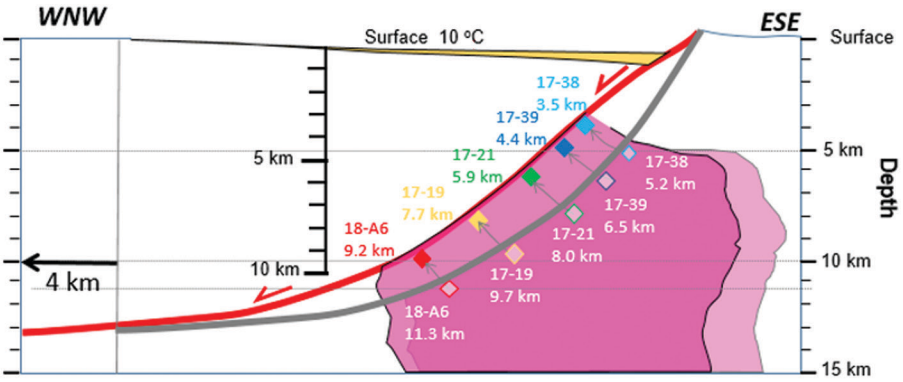

	~25 Ma Thermal Structure				Post-REH-1 Extension Geotherms (°C/km)								
Locality	Depth (km)	Temp. (°C) ~25 Ma	±	Geotherm ~25 Ma	Depth (km)	25	27.5	30	35	40	Temp. (°C) ~20 Ma	±	Geotherm ~20 Ma
RGD17-38	4.7	120	50	24.4	3	75	82.5	100	115	130	100	30	30.0
	5.2	120	50	22.0	3.5	87.5	96.25	115	132.5	150	100	30	25.7
	5.5	120	50	20.0	4.0	100	110	130	150	170	100	30	22.5
RGD 17-39	6.0	170	40	26.7	3.9	97.5	107	127	146.5	166	130	40	30.8
	6.5	170	40	24.6	4.4	110	121	142	164	186	130	40	27.3
	7.0	170	40	22.9	4.9	122.5	134.75	157	181.5	206	130	40	24.5
RGD 17-21	7.5	200	25	25.3	5.4	135	148.5	172	199	226	150	25	25.9
	8.0	200	25	23.8	5.9	147.5	162.25	187	216.5	246	150	25	23.7
	8.5	200	25	22.4	6.4	160	176	202	234	266	150	25	21.9
RGD 17-19	9.0	310	30	33.3	7	175	192.5	220	255	290	240	25	32.9
	9.7	310	30	30.9	7.7	192.5	211.75	241	279.5	318	240	25	29.9
	10.4	310	30	28.8	8.4	210	231	262	304	346	240	25	27.4
RGD18-A6	10.3	330	30	31.1	8.2	205	225.5	256	297	338	250	25	29.3
	11.3	330	30	28.3	9.2	230	253	286	332	378	250	25	26.1
	12.3	330	30	26.0	10.2	255	280.5	316	367	418	250	25	23.5

Figure 6. A possible kinematic model for the onset and evolution of REH-1 extension between ~25 and 21 Ma illustrating a plausible thermal evolution of the lower plate as a consequence of extension and isostatic uplift in the footwall of an initially listric normal fault (see discussion in text). "Before" state of cross-section (25 Ma) is lightly shaded; "after" state (21 Ma) is in color. Key assumptions of the model are itemized on the left, and the inferred thermal history from the kinematic model is compared with the observed cooling histories (from Figure 3) in the table underlying the diagram. Light blue shadings indicate the best matched thermal histories if extension began in the early Oligocene; light green shadings indicate the best matched thermal histories assuming initial extension bracketed between 21–25 Ma (See discussions in text).

zone, and thus may record the earliest stages of extension. We plan to obtain TnHe and ZHe data from this locality to evaluate this possibility more fully.

The intermediate temperature systems appear to be especially important in bracketing the progression of initial extension. First, note the large age-range bars for the 250°C isotherm from the samples from the western half of the pluton (RGD18-A6 and 17-19) (Figure 5). This is because both samples reached 250°C contemporaneously at ~23–6 Ma, but then remained within the 200–250°C temperature window for the next several million years before continuing to cool through the lower temperature range, starting after 21 Ma for RGD17-19 and after 17.5 Ma for RGD18-A6 (Figures 3 and 4). Sample RGD17-21 shows an analogous pattern, but at lower temperatures–initially cooling to 200°C at approximately 27 Ma, and then stabilizing in the 170–210°C window until cooling re-accelerated after ~23 Ma, coincident with the mean TnHe cooling age from the same locality. We interpret this as recording the REH-1 stage of extension proposed above.

To test the viability of the hypothesized latest Oligocene to earliest Miocene extensional pulse Figure 6 presents a simple kinematic model for the progression of REH-1 extension. We assume approximately 4 km of horizontal extension accommodated on a listric initial fault geometry flattening into the seismic/aseismic transition zone at ~13 km depth, using the inferred geometry of the 2008 Wells earthquake fault as an analog (Figure 6) (Smith and others, 2011). Based on regional geologic constraints summarized in the introduction, we infer that the fault must have daylighted at approximately 30 km up-dip from the REHW baseline (Figures 1 and 2). The listric fault geometry we assumed yields pre-extensional paleodepth estimates ranging from ~11.3 km for sample RGD18-A6 to ~5.2 km for

sample RGD17-38. These estimates resemble those of Colgan and others (2010), though generally ~500–1000 m deeper. Using this model we located the position of each of the analyzed samples and estimated the temperature of each at 25 Ma, our proposed initiation time for REH-1 extension. The estimated paleodepths and temperatures suggest geothermal gradients ranging from 22–33°C/km—similar to the modern Basin and Range geotherm.

We then imposed 4 km of extension assuming that the room problem between the two plates was accommodated mostly by isostatically-driven upward flexure of the lower plate as extension proceeds (i.e., the "rolling hinge model") (e.g., Lavellier and others, 1999). The remainder of the room problem was accommodated by ~1 km of hanging wall collapse. We assumed that extension accumulated at a constant rate of 1 km/m.y. until it stalled at ~21 Ma, and we then estimated temperatures based on their new depths and assuming a range of geothermal gradients from 25–40°C (Figure 6). Assuming this initial phase was complete and geotherms had stabilized by ~20 Ma, the results in the central part of the table in Figure 6 can be compared with the inferred temperature estimates for each of the samples at ~20 Ma, with the best-fit solutions highlighted in green. Although these assumptions yield non-unique solutions, it would be difficult to reproduce the observed thermal histories without invoking significant extension during the earliest Miocene to latest Oligocene time frame. Conversely, if extension continued at the same rate of 1 km/m.y. over the entire 8 m.y. time span from ~25–17 Ma, it would be extremely difficult not to force a wide area of the pluton through AFT and AHE closure temperatures. Either there must be a break in the continuity of extension or this early phase of extension must have proceeded much more slowly. The observed inflections in the cooling histories (Figure 3) favor the former alternative.

Finally, we can ask whether there is a stratigraphic record for the proposed REH-1 extensional phase. Lund-Snee and Miller (2015) document an approximately 300 m thick sequence of coarse cross bedded sandstone at the base of the Humboldt Formation near Indian Well at the north end of Cedar Ridge, with the basal beds yielding a minimum depositional age of 24.4 Ma based on detrital zircon and with a younger age bracket placed by $^{40}Ar/^{39}Ar$ sanidine ages of 15.51 ± 0.44 and 15.78 ± 0.45 Ma from immediately overlying tuff. Although these relationships do not preclude an age between 16 and 17 Ma for this subunit, we suggest that it represents a potential record of REH-1 syntectonic sedimentation. In addition, Satarugsa and Johnson (2000) interpret a wedge of chaotic reflectors at ~1 km depth on the west flank of Harrison Pass as a probable alluvial fan or megabreccia wedge. Interpreted from seismic line CT-1 (Satarugsa and Johnson, 2000), this unit is sandwiched between the upper "Indian Wells Formation" (probable Late Eocene tuff of Dixie Creek) (Lund Snee and others, 2016) and the basal Humboldt Formation. Thus, it represents another candidate for REH-1 syntectonic deposition. Finally, much farther north, recent mapping has documented megabreccia masses introduced at ~21 Ma into the sedimentary sequence of Clover Creek, a unit underlying the basal Humboldt Formation and overlying the 28-Ma tuff of Coal Mine Canyon (Henry and others, 2012; McGrew and Snoke, 2015)—thus documenting an analogous record elsewhere in the REHW. If the REH-1 phase extension reactivated pre-existing Wood Hills phase extensional structures, then this phase of extension may similarly be more strongly developed in the northern half of the REHW than it is in the Harrison Pass area. Most of the extensional mylonitization in the northern half of the REHW is bracketed between ~29 Ma and ~21 Ma (Wright and Snoke, 1993; McGrew and Snee, 1994).

Regardless of the interpretation of the pre-17.5 Ma cooling history, there can be little doubt that extension surged dramatically after ~17.5 Ma, as previously detailed by Colgan and others (2010). We will refer to this as "REH-2" extension to distinguish it from the pre-20 Ma extensional history discussed above. Our new results offer additional support for this inference based on KfAr isochrons regressed over the lower temperature steps and inflections in modeled cooling histories bracketed between 17 and 18 Ma (Figure 3b-d). With the exception of the easternmost samples, nearly the entire pluton cooled through AFT and AHe closure between 17 Ma and 10 Ma (Figure 4). However, there appears to be a likely inflection to a steeper slope on the time-distance graph east of ~22 km up-dip distance (Figure 4). This inference is also supported by the model presented in Figure 6, which would place everything southeast of sample 17-21 at or just-above the AFT and AHe closure temperature range at 17 Ma. At predicted paleodepths of < 4.5 km at 18 Ma, practically any extension would be sufficient to close the AFT system and very likely the AHe systems in the upper part of the pluton.

In light of the above relationships, we regressed only the data west of 22 km in order to obtain an estimate for the extension rate during the REH-2 extensional phase (Figure 4). Both the AFT and AHe data yield identical regressed age gradients of 2 km/m.y. If maintained at this rate over the entire 7 m.y. period from 17–10 Ma, this would yield ~14 km of extension (assuming an average 45° fault dip)—enough to nearly fully exhume the entire width of the southern Ruby Mountains. In this context, we note that the stratigraphic record from the Robinson Mountain volcanic field to the west suggests that the greatest rate of accumulation of the Miocene Humboldt Formation (> 1 km of sedimentary and volcanic strata) was bracketed between 15.8 and 12.4 Ma (Lund Snee and Miller, 2015; Lund Snee and others, 2016). We suggest 10–14 km of extension during the REH-2 phase, and an additional 3–5 km predating it in the REH-1 phase. Allowing an additional 3–5 km of extension after 10 Ma (Basin and Range extension) and 0–4 km of extension during the Late Eocene, total extension across the Harrison Pass area was probably in the range of 16–28 km. Our favored estimate is 22 ± 6 km of total extension. This would effectively restore Cedar Ridge to the western margin of the modern Ruby Mountain range front at Harrison Pass, with the strata underlying Huntington Valley restoring to a position overlying the Harrison Pass pluton.

Tectonic Implications

Late Eocene to Oligocene Tectonics (Wood Hills Phase)

The lack of appreciable Late Eocene to early Oligocene extension at the latitude of Harrison Pass poses the problem of how to reconcile these relationships with evidence for major Late Eocene extension farther north, centered on the Wood Hills (Figure 1). We suggest that the Wood Hills phase extension died out southward and that the younger REHW extensional system nucleated on the older, Wood Hills phase detachment fault farther north and then propagated southward into previously unextended or only weakly extended terrain, thus capturing and exhuming the Harrison Pass pluton during the REH-1 and REH-2 extensional phases detailed above. A number of other observations support the plausibility of this interpretation:

1. The west-east width of the exhumed metamorphic/plutonic domain is much greater to the north (≥ 30 km) than it is to the south (15–20 km) (Figure 1).
2. The extensional mylonitic shear zone thins and disappears from Harrison Pass southward, suggesting that both displacement and/or temperature conditions during exhumation diminish southward.
3. Thermobarometric constraints suggest exhumation of the metamorphic rocks from much greater paleodepths to the north than to the south. Specifically, kyanite-bearing pelitic assemblages in the East Humboldt Range and the Wood Hills record peak PT conditions ranging from 625°C, 6 kb to 775°C, 10 kb (Wills, 2014; McGrew and others, 2000; Hallett and Spear, 2014 and 2015). In contrast, andalusite-bearing assemblages in the contact aureole of the Harrison Pass pluton preclude pressures >4 kb near the southern end of the REHW—equivalent to paleodepths < 15 km (Barnes and others, 2001), and consistent with the pre-extensional burial depths inferred from stratigraphic reconstruction of the country rock into which the pluton intrudes (Colgan and others, 2010).
4. The depositional basin to the west of the REHW is divided into two distinct subbasins—the deeper (locally > 4 km) and more regionally extensive Lamoille-Starr Valley subbasin north of the Lamoille salient vs. the smaller Huntington Valley subbasin to the west of the Harrison Pass area (Satarugsa and Johnson, 2000). This suggests the possibility of a tectonic discontinuity between the Lamoille salient and Harrison Pass.

We note that the total width of the extended terrain plus the adjacent basin to the west narrows abruptly south of line 45S in Figure 1, from ~66 km to ~ 46 km. This suggests the hypothesis that the Wood Hills phase extension may have largely terminated in a now-buried NW-trending left-lateral strike-slip boundary subparallel to this line. This also correlates with the transition zone from the Lamoille subbasin in the north to the Huntington subbasin in the south (Satarugsa and Johnson, 2000).

Regardless of the above relationships, while it is difficult to establish any Eocene extension at the latitude of Harrison Pass, it is also difficult to exclude the possibility of a small amount of extension (no more than 3–4 km). The distribution of the Late Eocene Elko Formation and the overlying Tuff of Dixie Creek supports this possibility. The occurrence of 500–1000 m of these units in well logs in Huntington Valley shows that they were probably deposited over the Harrison Pass area before being translated westward to their current location. Yet there is no evidence for their deposition over Medicine Mountain or the Maverick Springs Range to the east. On the contrary, the deposition of mid-Miocene Humboldt formation directly on the Upper Paleozoic strata of Medicine Mountain and the Maverick Springs Range suggests that they were positive areas before the Miocene—a transition that is most easily explained if they were in the uplifted footwall of a normal fault bounding the eastern side of the Elko Basin. Furthermore, recent investigation of the detrital zircon geochronology of the Elko Formation strongly suggests a transition to extension between 43–42 Ma based on an influx of sediment with dramatically reduced lag times between U-Pb zircon and (U-Th)/He zircon double dates (Canada and others, 2020).

Late Oligocene to Miocene Tectonics (REH-phase)

Regardless of the earlier tectonic history, the vast majority of extension at the latitude of Harrison Pass clearly occurred during the Miocene. As summarized above, this may have included up to 4 km of extension accumulated between 25–21 Ma ("REH-1") followed by 10–14 km extension accumulated between 17.5 and ~ 11 Ma ("REH-2"). The tectonic trigger for REH-1 phase extension is unclear, but we note the temporal correspondence of this event with major extension farther south in Nevada and in the Arizona metamorphic core complexes (e.g., Singleton and others, 2014; Long and others, 2018; Spencer and others, 2019). The initiation of extension during this time frame may have been triggered by the relaxation of contractional boundary conditions following the initiation and early growth of the San Andreas transform margin. In particular, we note the approximate coincidence in timing with the inferred subduction of the Pioneer fracture zone, which would have abruptly lengthened the transform margin and introduced a slab window (e.g., Severinghaus and Atwater, 1990). We suggest the possibility that rifting that initiated farther south at the latitude of the growing transform margin may have penetrated farther north and deeper into the interior of the Cordillera than has been widely appreciated. This phase of extension may have nucleated on pre-existing Late Eocene structures and thus may have focused into a relatively narrow zone centered on the REHW.

The tectonic trigger for post-17.5-Ma (REH-2) regional extension across northern Nevada has previously been attributed to impingement of NW Nevada over the Yellowstone thermal plume (Colgan and Henry, 2009; Colgan and others, 2010; Camp and others, 2015). Intriguingly, the deeper level samples (especially RGD18-A6, Figure 3d) appear to preserve evidence

for a thermal pulse peaking at 17.5 Ma immediately before the onset of REH-2 extension. This possible heating event is consistent with the hypothesis that the arrival of the Yellowstone hotspot may have been the key trigger for the onset of this phase of extension. In the REHW a widespread (though not voluminous) suite of basaltic dikes also approximately coincides with this possible thermal event. We note that such a nonlinearity in the thermal history could also help to explain some of the discordances in the data. For example, potentially resetting all thermochronometers at deeper structural levels but resetting progressively lower temperature thermochronometers at higher structural levels while not affecting areas that had already been exhumed and cooled to well below their closure temperatures.

We suggest that the relatively small amount of extension associated with the REH-1 phase (and possibly also with the older Wood Hills extensional phase discussed above) indicates that the crust was probably on the brink of extensional collapse from the Late Eocene onward. In this conception, the arrival of the Yellowstone hotspot played a pivotal role by introducing a thermal pulse that weakened the crust and triggered the release of long-standing extensional boundary conditions and the acceleration in extension observed after 17.5 Ma. That extension continues to the present day, though at a greatly reduced rate, as expressed by the Basin and Range extensional phase.

CONCLUSIONS

The southern Ruby Mountains, at the latitude of Harrison Pass, were exhumed by up to four episodes of extension. If present at all, the earliest extensional phase, the Late Eocene "Wood Hills" phase, is much less significant than it appears to be in the northern half of the REHW because it was insufficient to trigger the closure of major thermochronometric systems. Thus, this early phase of extension must have been relatively concentrated and localized to the northern REHW. At Harrison Pass it could have accommodated no more than ~4 km of horizontal extension.

The thermochronometric record of extensional exhumation appears to begin with an as-yet poorly defined latest Oligocene—earliest Miocene extensional phase (here termed "REH-1") recorded by cooling of midrange thermochronometers (TnHe, ZHe and KfAr) between ~21 and ~25 Ma. REH-1 phase extension probably was not great in magnitude (< 5 km) and either proceeded at a slow rate << 1 km/m.y. or, more likely, stalled after ~20 or 21 Ma. Though the tectonic trigger of this phase is unclear, we suggest that it may correlate with similar-aged extension farther south in the Cordillera that may relate to evolving far-field boundary conditions associated with the establishment and early lengthening of the San Andreas transform.

The main extensional phase (REH-2) began after 17.5 Ma and proceeded rapidly (~2 km/m.y.) until ~11 Ma. The initiation of this pulse of extension correlates closely with the arrival of the Yellowstone hot spot in northwestern Nevada, and the deeper level KfAr samples investigated here suggest a possible thermal pulse peaking at 17.5 Ma immediately before the onset of REH-2 extension. In total, REH-2 probably accommodated at least 10 km of horizontal displacement and was primarily responsible for the exhumation and eastward-tilting of the Harrison Pass pluton. Much slower, post-10 Ma Basin and Range extension brings the history to date. Total extension across the Harrison Pass area likely was between 16 and 28 km, with a preferred estimate of 22 km. Taken together, the new results support the prior synthesis of Colgan and others (2010) with the addition of the previously unrecognized REH-1 phase extension. We suggest that the crust of the northern Basin and Range province was primed for collapse from the Late Eocene onward, but that regional (as opposed to localized) collapse awaited the thermal weakening of the crust associated with the arrival of the Yellowstone thermal plume (Colgan and Henry, 2009).

ACKNOWLEDGMENTS

We gratefully acknowledge financial support from NSF Award EAR-1728537: "Collaborative Research: Documenting the transition from contraction to extension in the Ruby-East Humboldt-Wood Hills Metamorphic Core Complex, Southwestern U.S. Cordillera." In addition, we wish to acknowledge invaluable assistance from Carrie Bruno-Meisner and our field assistants: Amaris Rodgers, Alex Carte, Joseph Jeruc and Gardner Dennis from the University of Dayton and Nicole Gonzalez and Carlton Mueller from the University of Colorado-Boulder. We also gratefully acknowledge the support of Terry Spell and Kathleen Zanetti at the Nevada Isotope Geochronology Laboratory (University of Nevada-Las Vegas) for the KfAr analyses. We also thank Andrew Zuza, Fleetwood Koutz, and William Pennell for excellent technical and editorial reviews that greatly improved this manuscript.

REFERENCES

Armstrong, R.L., 1968, Sevier orogenic belt in Nevada and Utah: Geological Society of America Bulletin, 79, pp.429–458.

Barnes, C. G., B. R. Burton, T. C. Burling, J. E. Wright, and H. R. Karlsson, 2001, Petrology and geochemistry of the late Eocene Harrison Pass pluton, Ruby Mountains core complex, Nevada: J. Petrol., v. 42, p. 901–929.

Blackwell, D.D., 1983, Heat flow in the northern Basin and Range province, Geothermal Resources Council Special Report, 13, pp.81–92.

Brooks, W.E., Thorman, C.H. and Snee, L.W., 1995, The $^{40}Ar/^{39}Ar$ ages and tectonic setting of the middle Eocene northeast Nevada volcanic field: Journal of Geophysical Research: Solid Earth, 100(B6), pp.10403–10416.

Burton, B. R., 1997, Structural geology and emplacement history of the Harrison Pass pluton, central Ruby Mountains, Nevada: University of Wyoming, Laramie, Wyoming, Ph.D. thesis, 295 p.

Camp, V.E., Pierce, K.L., and Morgan, L.A., 2015, Yellowstone plume trigger for Basin and Range extension and coeval emplacement of the Nevada-Columbia Basin magmatic belt: Geosphere, v. 11, p. 203–225, doi:10.1130/GES01051.

Canada, A.S., Cassel, E.J., Stockli, D.F., Smith, M.E., Jicha, B.R. and Singer, B.S., 2020, Accelerating exhumation in the Eocene North American

Cordilleran hinterland: Implications from detrital zircon (U-Th)/(He-Pb) double dating: Geological Society of America Bulletin, v. 32, p. 198–214.

Coats, R.R., 1987, Geology of Elko County, Nevada: Reno, Nevada Bureau of Mines and Geology Bulletin 101, 112p.

Colgan, J.P. and Henry, C.D., 2009. Rapid middle Miocene collapse of the Mesozoic orogenic plateau in north-central Nevada: International Geology Review, 51(9–11), pp. 920–961.

Colgan, J.P., Howard, K.A., Fleck, R.J., and Wooden, J.L., 2010, Rapid middle Miocene extension and unroofing of the southern Ruby Mountains, Nevada: Tectonics, v. 29, TC6022, doi:10.1029/2009TC002655.

Coney, P.J., 1980, Cordilleran metamorphic core complexes - An Overview, *in* Crittenden, M.D., Coney, P.J., and Davis, G.H., editors, Cordilleran Metamorphic Core Complexes: Geological Society of America, Memoir 153, p. 7–27.

Dallmeyer, R.D., Snoke, A.W., McKee, E.H., 1986, The Mesozoic-Cenozoic tectonothermal evolution of the Ruby Mountains, East Humboldt Range, Nevada: a Cordilleran metamorphic core complex: Tectonics, v. 5, p. 931–954.

Dokka, R.K., Mahaffie, M.J., and Snoke, A.W., 1986, Thermochronologic evidence of major tectonic denudation associated with detachment faulting, northern Ruby Mountains-East Humboldt Range, Nevada: Tectonics, v. 5, p. 995–1006.

Gans, P.B. and Miller, E.L., 1983. Style of mid-Tertiary extension in east-central Nevada: Utah Geological and Mineralogical Survey Special Studies, v. 59.

Gonzalez, N., Metcalf, J. R., McGrew, A. J., 2019, Thermochronology of upper crustal rocks in the Wood Hills, Nevada: Documenting the transition from contraction to extension in the U.S. Cordillera: Annual Meeting, Geological Society of America, Phoenix, AZ

Hallett, B.W., and Spear, F.S., 2014, The P–T history of anatectic pelites of the northern East Humboldt Range, Nevada: Evidence for tectonic loading, decompression, and anatexis: Journal of Petrology, v. 55, p. 3–36.

Hallett, B.W. and Spear, F.S., 2015, Monazite, zircon, and garnet growth in migmatitic pelites as a record of metamorphism and partial melting in the East Humboldt Range, Nevada: American Mineralogist, 100(4), pp. 951-972.

Harrison, T.M., Duncan, I.A.N. and Mcdougall, I.A.N., 1985. Diffusion of 40Ar in biotite: temperature, pressure and compositional effects. Geochimica et Cosmochimica Acta, 49(11), pp.2461-2468.

Henry, C.D., McGrew, A.J., Colgan, J.P., Snoke, A.W., and Brueseke, M.E., 2011, Timing, distribution, amount, and style of Cenozoic extension in the northern Great Basin, *in* Lee, J., and Evans, J. P., eds., Geologic Field Trips to the Basin and Range, Rocky Mountains, Snake River Plain, and Terranes of the U.S. Cordillera: Geological Society of America Field Trip Guide 21, pp. 27–66.

Henry, C.D., Hinz, N.H., Faulds, J.E., Colgan, J.P., John, D.A., Brooks, E.R., Cassel, E.J., Garside, L.J., Davis, D.A., and Castor, S.B., 2012, Eocene–Early Miocene paleotopography of the Sierra Nevada–Great Basin–Nevadaplano based on widespread ash-flow tuffs and paleovalleys: Geosphere, v. 8, no. 1, pp. 1–27, doi:10.1130/GES00727.1.

Henry, C.D. and John, D.A., 2013, Magmatism, ash-flow tuffs, and calderas of the ignimbrite flareup in the western Nevada volcanic field, Great Basin, USA: Geosphere, v. 9, pp. 951–1008.

Hess, R.H., Henson, M.A., Davis, D.A., Limerick, S.H., Siewe, S.S., and Niles, M., 2011, Oil and gas well information for Nevada—2011 update: Reno, NV, Nevada Bureau of Mines and Geology, Open-file Report 11-6, Online, http://www.nbmg.unr.edu/Oil&Gas/WellSearch.html, accessed December, January, 2019-20.

Hiess, J., Condon, D.J., McLean, N. and Noble, S.R., 2012, $^{238}U/^{235}U$ systematics in terrestrial uranium-bearing minerals. Science, 335(6076), pp.1610–1614.

Hodges, K.V., Snoke, A.W. and Hurlow, H.A., 1992, Thermal evolution of a portion of the Sevier hinterland: the northern Ruby Mountains-East Humboldt Range and Wood Hills, northeastern Nevada: Tectonics, 11(1), pp.154–164.

Howard, K.A., 1980, Metamorphic infrastructure in the northern Ruby Mountains, Nevada, *in* Crittenden, M.D., Jr., Coney, P.J., and Davis, G.H., eds., Cordilleran Metamorphic Core Complexes, Geological Society of America Memoir 153, p. 335–347.

Howard, K.A., 2003, Crustal structure *in* the Elko-Carlin region, Nevada, during Eocene gold mineralization: Ruby-East Humboldt metamorphic core complex as a guide to the deep crust: Economic Geology and the Bulletin of the Society of Economic Geologists, v. 98, p. 249–268.

Hudec, M. R.,1992, Mesozoic structural and metamorphic history of the central Ruby Mountains metamorphic core complex, Nevada, Geol. Soc. Am. Bull., 104, 1086–1100.

Hurlow, H.A., Snoke, A.W. and Hodges, K.V., 1991, Temperature and pressure of mylonitization in a Tertiary extensional shear zone, Ruby Mountains-East Humboldt Range, Nevada: Tectonic implications: Geology, v. 19(1), pp. 82–86.

Jeruc, J. W., Carte, A. J., McGrew, A. J., Metcalf, J. R., 2019, A two-pulse cooling history of Late Eocene to Miocene extensional exhumation from the southern East Humbloldt Range Metamorphic core complex, Nevada: Cordilleran Section Meeting, Geological Society of America, Portland, OR.

Johnson, J.G. and Pendergast, A., 1981, Timing and mode of emplacement of the Roberts Mountains allochthon, Antler orogeny: Geological Society of America Bulletin, 92(9), pp. 648–658.

Jones, J.V., III, 1999, Deformational, magmatic and metamorphic history of the central Ruby Mountains, Elko County, Nevada: Laramie, Wyoming, The University of Wyoming, M.S. Thesis, 166 p.

Ketcham, R.A., Donelick, R.A. and Carlson, W.D., 1999. Variability of apatite fission-track annealing kinetics: III. Extrapolation to geological time scales. American Mineralogist, 84(9), pp.1235–1255.

Ketcham, R.A., Gautheron, C. and Tassan-Got, L., 2011. Accounting for long alpha-particle stopping distances in (U–Th–Sm)/He geochronology: refinement of the baseline case. Geochimica et Cosmochimica Acta, 75(24), pp. 7779–7791.

Ketcham, R.A., 2014. HeFTy Versions 1.8.3 – Users Manual.

Ketner, K.B.,1998,The nature and timing of tectonism in the western facies terrane of Nevada and California: an outline of evidence and interpretations derived from geologic maps of key areas: (No. 1592). US Geological Survey Professional Paper 1592, 19 p.

Kistler, R.W., Ghent, E.D., and O'Neil, J.R., 1981, Petrogenesis of garnet two-mica granites in the Ruby Mountains, Nevada: Journal of Geophysical Research, v. 86, pp. 10, 591–10, 606.

Lavellier, L.L., Buck, W.R., Poliakov, A.N.B., 1999, Self-consistent rolling-hinge model for the evolution of large-offset low-angle normal faults: Geology, 27 (12): 1127–1130. doi: https://doi.org/10.1130/0091-7613(1999)027<1127:SCRHMF>2.3.CO;2

Long, S.P., 2012, Magnitudes and spatial patterns of erosional exhumation in the Sevier hinterland, eastern Nevada and western Utah, USA; insights from a Paleogene paleogeologic map: Geosphere, v. 8, pp. 881–901, doi: 10.1130/GES00783.1.

Long, S.P., 2015, An upper-crustal fold province in the hinterland of the Sevier orogenic belt, eastern Nevada, U.S.A.: A Cordilleran Valley and Ridge in the Basin and Range: Geosphere,v. 11, No. 2, p. 404–424. doi: https://doi.org/10.1130/GES01102.1

Long, S. P., Heizler, M. T., Thomson, S. N., Reiners, P. W., & Fryxell, J. E., 2018, Rapid Oligocene to early Miocene extension along the Grant

Range detachment system, Nevada, USA: Insights from multipart cooling histories of footwall rocks: Tectonics, 37, 4752– 4779. https://doi.org/10.1029/2018TC005073

Lovera, O.M., Richter, F.M., and Harrison, T.M., 1989. The $^{40}Ar/^{39}Ar$ thermochronometry for slowly cooled samples having a distribution of diffusion domain sizes. Journal of Geophysical Research, 94 (12), 17,917–17, 935.

Lovera, O. M., Richter, F. M., & Harrison, T. M., 1991, Diffusion domains determined by ^{39}Ar released during step heating: Journal of Geophysical Research: Solid Earth, 96(B2), 2057–2069.

Lovera, O.M., Grove, M., Harrison, T.M. and Mahon, K.I., 1997, Systematic analysis of K-feldspar $^{40}Ar^{39}Ar$ step heating results: I. Significance of activation energy determinationsL Geochimica et Cosmochimica Acta, 61(15), pp. 3171–3192.

Lovera, O.M., Grove, M. and Harrison, T.M., 2002. Systematic analysis of K-feldspar $^{40}Ar/^{39}Ar$ step heating results II: Relevance of laboratory argon diffusion properties to nature. Geochimica et Cosmochimica Acta, 66(7), pp. 1237–1255.

Lund Snee, J.-E., Miller, E.L., 2015, Preliminary geologic map of the Cenozoic units of central Robinson Mountain volcanic field and northwestern Huntington Valley, Elko County, Nevada, Nevada Bureau of Mines and Geology

Lund Snee, J.-E. Miller, E.L., Grove, M., Hourigan, J.K., Konstantinou, A., 2016, Cenozoic paleogeographic evolution of the Elko Basin and surrounding region, northeast Nevada. Geosphere; 12 (2): 464–500. doi: https://doi.org/10.1130/GES01198.1

McDougall, I., and Harrison, T.M., 1999, Geochronology and Thermochronology by the $^{40}Ar/^{39}Ar$ Method: Oxford University Press, on demand.

McGrew, A.J., and Snee, L.W., 1994, $^{40}Ar/^{39}Ar$ thermochronologic constraints on the tectonothermal evolution of the northern East Humboldt Range metamorphic core complex, Nevada: Tectonophysics, v. 238, pp. 425–450.

McGrew and Snoke, 2015, Geologic Map of the Welcome quadrangle and an adjacent part of the Wells quadrangle, Elko County, Nevada: Nevada Bureau of Mines and Geology Map 184, scale 1:24,000, 40 p.

McGrew, A.J., Peters, M.T., and Wright, J.E., 2000, Thermobarometric constraints on the tectonothermal evolution of the East Humboldt Range metamorphic core complex, Nevada: Geological Society of America Bulletin, v. 112, pp. 45–60.

McGrew, A. J., Metcalf, J. R., Jeruc, J. W., Carte, A. J., Meisner, C. B., 2019, The Late Eocene to Miocene cooling and exhumation of the Ruby Mountains—East Humboldt Range metamorphic core complex, Nevada: New $^{40}Ar/^{39}Ar$ thermochronologic Constraints: Annual Meeting, Geological Society of America, Phoenix, Paper 216-12,21, Geological Society of America Abstracts with Programs. V. 51, No. 5 doi: 10.1130/abs/2019AM-339225

Metcalf, J. R., McGrew, A. J., Meisner, C. B., 2018, Exhumation of a Metamorphic Core Complex: Apatite and zircon (U-Th)/He constraints on the timing and rate of cooling of the Ruby Mountains—East Humboldt—Wood Hills Metamorphic Core Complex, northeastern Nevada: 2018 International Conference on Thermochronology, Quedlinburg, Germany

Metcalf, J. R., McGrew, A. J., Mueller, C., Meisner, C. B., 2019, The Oligocene-Miocene cooling and exhumation of a Cordilleran metamorphic core complex—New apatite, zircon and titanite (U-Th)/He thermochronology from the Ruby Mountains, Nevada: Annual Meeting, Geological Society of America, Phoenix, AZ.

Murray, K.E., Braun, J. and Reiners, P.W., 2018, Toward robust interpretation of low-temperature thermochronometers in magmatic terranes: Geochemistry, Geophysics, Geosystems, v. 19(10), pp. 3739–3763.

Pape, J.R., Seedorff, E., Baril, T.C. and Thompson, T.B., 2016, Structural reconstruction and age of an extensionally faulted porphyry molybdenum system at Spruce Mountain, Elko County, Nevada: Geosphere, 12(1), pp. 237–263.

Ponce, D.A., Watt, J.T., and Bouligand, C. 2011, Geophysical Setting of the February 21, 2008 Mw 6.0 Wells Earthquake, Nevada, Implications for Earthquake Hazards, *in* dePolo, C.M., and LaPointe, D.D., eds., The 21 February 2008 Mw 6.0 Wells, Nevada earthquake—a compendium of earthquake-related investigations prepared by the University of Nevada, Reno (online version): Nevada Bureau of Mines and Geology Special Publication 36, pp. 89–100.

Reese, N. M. (1986), Cenozoic tectonic history of the Ruby Mountains and adjacent areas, Northeastern Nevada— Constraints from radiometric dating and seismic profiles: Southern Methodist Univ., Dallas, TX, M.S. thesis, 87 pp.

Satarugsa, P. and Johnson, R.A., 2000, Cenozoic tectonic evolution of the Ruby Mountains metamorphic core complex and adjacent valleys, northeastern Nevada: Rocky Mountain Geology, 35(2), pp. 205–230.

Severinghaus, J. and Atwater, T., 1990, Cenozoic geometry and thermal state of the subducting slabs beneath western North America: Basin and range extensional tectonics near the latitude of Las Vegas, Nevada, Geological Society of America Memoir, 176, pp. 1–22.

Singleton, John S., Daniel F. Stockli, Phillip B. Gans, and Michael G. Prior, 2014, Timing, rate, and magnitude of slip on the Buckskin-Rawhide detachment fault, west central Arizona: Tectonics 33, no. 8, 1596–1615.

Smith, K., Pechmann, J., Meremonte, M. and Pankow, K., 2011, Preliminary analysis of the Mw 6.0 Wells, Nevada, earthquake sequence: Geol. Spec. Publ., 36, pp.127–145.

Snoke, A.W., 1980, Transition from infrastructure to suprastructure in the northern Ruby Mountains, Nevada, *in* Crittenden, M.D., Jr., Coney, P.J., and Davis, G.H., eds., Cordilleran metamorphic core complexes: Boulder, Colorado, Geological Society of America Memoir 153, pp. 287–333.

Snoke, A.W., and Miller, D. M., 1988, Metamorphic and tectonic history of the northeastern Great Basin, *in* Ernst, W. G., ed., Rubey Volume No. VII, Metamorphism and crustal evolution of the western United States: Prentice-Hall, pp. 606–648.

Snoke, A.W., McGrew, A.J., Valasek, P.A., and Smithson, S.B., 1990, A crustal cross-section for a terrain of superimposed shortening and extension: Ruby Mountains-East Humboldt Range metamorphic core complex, Nevada, *in* Salisbury, M.H., and Fountain, D.M., eds., Exposed cross-sections of the continental crust: Dordrecht, The Netherlands, Kluwer Academic Publishers, pp. 103–135.

Snoke, A.W., Howard, K.A., McGrew, A.J., Burton, B.R., Barnes, C.G., Peters, M.T., and Wright, J.E., 1997, The grand tour of the Ruby–East Humboldt metamorphic core complex, northeastern Nevada: Part 1—Introduction & Road Log, *in* Link, P.K., and Kowallis, B.J., eds., Proterozoic to Recent stratigraphy, tectonics, and volcanology, Utah, Nevada, southern Idaho and central Mexico: Provo, Utah, Brigham Young University Geology Studies, v. 42, Part 1, pp. 225–269.

Spell, T.L., McDougall, I., 2003, Characterization and calibration of $^{40}Ar/^{39}Ar$ dating standards: Chemical Geology, v. 198, pp. 189–211.

Spencer, J. E., Richard, S. M., Lingrey, S. H., Johnson, B. J., Johnson, R. A., & Gehrels, G. E., 2019, Reconstruction of mid-Cenozoic extension in the Rincon Mountains area, southeastern Arizona, USA, and geodynamic implications, Tectonics, 38, 2338– 2357. https://doi.org/10.1029/2019TC005565

Staudacher, T.H., Jessberger, E.K., Dorflinger, D., and Kiko, J., A refined ultrahigh-vacuum furnace for rare gas analysis, Journal of Physics E: Scientific Instruments, 11, 781–784, 1978.

Sullivan, W.A., and Snoke, A.W., 2007, Comparative anatomy of core-complex development in the northeastern Great Basin, U.S.A.: Rocky Mountain Geology, v. 42, p. 1–29.

Thorman, C.H. and Peterson, F., 2003, The Middle Jurassic Elko Orogeny: A major tectonic event in Nevada-Utah: Annual Meeting Expanded Abstracts American Association of Petroleum Geologists, Vol. 12, pp. 169–174. Tulsa, Okla.

Trexler, J. H., Cashman, P.H., Snyder, W.S., Vladimir I. Davydov, V.I., 2004, Late Paleozoic tectonism in Nevada: Timing, kinematics, and tectonic significance: Geological Society of America Bulletin, v. 116 (5-6), pp. 525–538. doi: https://doi.org/10.1130/B25295.1

Vermeesch, P., 2018, IsoplotR— a free and open toolbox for geochronology: Geoscience Frontiers, v. 9, pp. 1479–1493.

Wendt, I., and Carl, C., 1991, The statistical distribution of the mean squared weighted deviation: Chemical Geology, v. 86, pp. 275–285.

Whittington, A., Hofmeister, A. & Nabelek, P., 2009, Temperature-dependent thermal diffusivity of the Earth's crust and implications for magmatism: Nature, v. 458, p. 319–321. https://doi.org/10.1038/nature07818

Wills, M.A., 2014, A metamorphic pressure-temperature time path from the Wood Hills, Elko County, eastern Nevada: M.S. Thesis, Northern Arizona University, Flagstaff, AZ, 81p.

Wolfe, F., Metcalf, J. R., McGrew, A. J., Rahl, J. M., 2016, New constraints on the timing, rate and style of exhumation of the Wood Hills and Pequop Mountains, Elko County, Nevada: Annual Meeting, Geological Society of America, Denver, CO.

Wolfe, F., and Rahl, J.M., 2016, New constraints on the timing, rate and style of exhumation of the Wood Hills and Pequop Mountains, Elko County, Nevada: 29th Annual Keck Symposium Short Contributions, Oberlin College, 7 p. https://keckgeology.org/wp-content/uploads/Wolfe.pdf

Wright, J.E., and Snoke, A.W., 1993, Tertiary magmatism and mylonitization in the Ruby-East Humboldt metamorphic core complex, northeastern Nevada: U-Pb geochronology and Sr, Nd, Pb isotope geochemistry: Geological Society of America Bulletin, v. 105, p. 935–952.

Zeitler PK, 1993, Inversion of $^{40}Ar/^{39}Ar$ age spectra using the controlled-random-search method. EOS 74:650.

Zeitler P.K., 2017, Arvert 6.1.1. Inversion of $^{40}Ar/^{39}Ar$ age spectra. User's Manual.

Zuza, A.V., Cao, W., Hinz, N.H., DesOrmeau, J.W., Odlum, M.L. and Stockli, D.F., 2019, Footwall rotation in a regional detachment fault system: Evidence for horizontal-axis rotational flow in the Miocene Searchlight pluton, NV, Tectonics, 38(7), pp. 2506–2539.

APPENDIX 1. ANALYTICAL METHODS

(U-Th)/He Methods

Analyses carried out at the University of Colorado Boulder TRaIL (Thermochronology Research and Instrumentation Lab) used the following methods. Individual mineral grains are handpicked using a Leica M165 binocular microscope equipped with a calibrated digital camera and capable of both reflected and transmitted, polarized light. The grains are screened for quality, including crystal size, shape, and the presence of inclusions. After characterization, grains are placed into small, acid cleaned Nb tubes that are then crimped on both ends. This Nb packet is then loaded into an ASI Alphachron He extraction and measurement line. The packet is placed in the UHV extraction line (~3×10^{-8} torr) and heated with a 25W diode laser to ~800–1100°C for 10 minutes to extract the radiogenic 4He. The degassed 4He is then spiked with approximately 13 ncc of pure 3He, cleaned via interaction with two SAES getters, and analyzed on a Balzers PrismaPlus QME 220 quadrupole mass spectrometer. This procedure is repeated at least once to ensure complete mineral degassing. Degassed grains are then removed from the line and taken to a Class 10 clean lab for dissolution.

Individual zircon and titanite grains are dissolved using Parr large-capacity dissolution vessels in a multi-step acid-vapor dissolution process. Grains (including the Nb tube) are placed in Ludwig-style Savillex vials, spiked with a ^{235}U – ^{230}Th – ^{145}Nd tracer, and mixed with 200 µl of Optima grade HF. The vials are then capped, stacked in a 125 mL Teflon liner, placed in a Parr dissolution vessel, and baked at 220°C for 72 hours. After cooling, the vials are uncapped and dried down on a 90°C hot plate until dry. The vials then undergo a second round of acid-vapor dissolution, this time with 200 µl of 6N Optima grade HCl in each vial that is baked at 200°C for 24 hours. Vials are then dried down a second time on a hot plate. Once dry, 200 µl of a 7:1 HNO_3:HF mixture is added to each vial, the vial is capped, and cooked on the hot plate at 90°C for 4 hours. Once the minerals are dissolved they are diluted with 3 mL of doubly-deionized water, and taken to the ICP-MS lab for analysis. Sample solutions, along with normal solutions and blanks, are analyzed for U, Th, and Sm content using an Agilent 7900 quadrupole ICP-MS. After the U, Th, and Sm contents are measured, He dates and all associated data are calculated on a custom spreadsheet using the methods described in Ketcham and others, (2011). The natural occurring $^{238}U/^{235}U$ ratio used in data reduction is 137.818 after Hiess and others (2012). Every batch of samples includes standards run sporadically throughout the process to monitor procedures and maintain consistency from run to run. Long term averages of Fish Canyon Tuff zircons and Durango fluorapatites run in the CU TRaIL are 28.7 ± 1.8 Ma (n = 150) and 31.1 ± 2.1 (n = 85), respectively.

$^{40}Ar/^{39}Ar$ K-feldspar Methods

Laboratory Methods

K-feldspar samples for analysis by the $^{40}Ar/^{39}Ar$ method were first disaggregated by hand and relatively inclusion free fragments selected from broken K-feldspar grains (megacrysts where possible). These fragments were then crushed by hand with a mortar and pestle, sieved, cleaned ultrasonically, and separated by conventional density separation methods before hand-picking the aliquots sent to the Nevada Isotope Geochronology Laboratory for final processing and analysis.

Samples analyzed by the $^{40}Ar/^{39}Ar$ method at the University of Nevada Las Vegas were wrapped in Al foil and stacked in 6 mm inside diameter sealed fused silica tubes. Individual packets averaged 3 mm thick and neutron fluence monitors (GA-1550 biotite) were placed every 5–10 mm along the tube. Synthetic K-glass and optical grade CaF_2 were included in the irradiation packages to monitor neutron induced argon interferences from K and Ca. Loaded tubes were packed in an Al container for irradiation. Samples irradiated at the U. S. Geo-

logical Survey TRIGA Reactor, Denver, CO were in-core for 10 hours in the 1 MW TRIGA type reactor. Correction factors for interfering neutron reactions on K and Ca were determined by repeated analysis of K-glass and CaF_2 fragments. Measured $(^{40}Ar/^{39}Ar)K$ values were 4.29 (± 7.89%) × 10^{-2}. Ca correction factors were $(^{36}Ar/^{37}Ar)Ca$ = 1.93 (± 0.59%) x 10^{-4} and $(^{39}Ar/^{37}Ar)Ca$ = 5.69 (± 0.25%) × 10^{-4}. J factors were determined by fusion of 4–8 individual crystals of GA-1550 biotite neutron fluence monitors which gave reproducibility's of 0.3% to 0.8% at each standard position. Matlab curve fit was used to determine J and uncertainty in J at each standard position. No significant neutron fluence gradients were present within individual packets of crystals as indicated by the excellent reproducibility of the single crystal GA-1550 biotite fluence monitor fusions.

Irradiated GA-1550 biotite standards together with CaF_2 and K-glass fragments were placed in a Cu sample tray in a high vacuum extraction line and were fused using a 20 W CO_2 laser. Sample viewing during laser fusion was by a video camera system and positioning was via a motorized sample stage. Samples analyzed by the furnace step heating method utilized a double vacuum resistance furnace similar to the Staudacher and others (1978) design. Reactive gases were removed by three GP-50 SAES getters prior to being admitted to a MAP 215-50 mass spectrometer by expansion. The relative volumes of the extraction line and mass spectrometer allow 80% of the gas to be admitted to the mass spectrometer for laser fusion analyses and 76% for furnace heating analyses. Peak intensities were measured using a Balzers electron multiplier by peak hopping through 7 cycles; initial peak heights were determined by linear regression to the time of gas admission. Mass spectrometer discrimination and sensitivity was monitored by repeated analysis of atmospheric argon aliquots from an on-line pipette system. Measured $^{40}Ar/^{36}Ar$ ratios were 321.98 ± 0.02% during this work, thus a discrimination correction of 0.9177 (4 AMU) was applied to measured isotope ratios. The sensitivity of the mass spectrometer was ~6 × 10^{-17} mol/mV with the multiplier operated at a gain of 36 over the Faraday. Line blanks averaged 2.84 mV for mass 40 and 0.01 mV for mass 36 for laser fusion analyses and 12.80 mV for mass 40 and 0.04 mV for mass 36 for furnace heating analyses. Discrimination, sensitivity, and blanks were relatively constant over the period of data collection. Computer automated operation of the sample stage, laser, extraction line and mass spectrometer as well as final data reduction and age calculations were done using LabSPEC software written by B. Idleman (Lehigh University). An age of 98.50 Ma (Spell and McDougall, 2003) was used for the GA-1550 biotite fluence monitor in calculating ages for samples.

To support the diffusion modeling described below potassium feldspar samples were run using tightly controlled heating schedules of 34 steps from 422–1398°C, including multiple replicate isothermal steps across the lower temperature range (< 800°C). None of the samples considered here yielded statistically consistent plateau ages (3 or more contiguous gas fractions having analytically indistinguishable ages at ± 2σ analytical error and comprising ≥ 50% of the released gas). Total gas (integrated) ages were calculated by weighting by the amount of ^{39}Ar released, whereas plateau ages are weighted by the inverse of the variance. For each sample inverse isochron diagrams were examined to check for the effects of excess argon. Reliable isochrons are based on the MSWD criteria of Wendt and Carl (1991) and, as for plateaus, must comprise contiguous steps and a significant fraction of the total gas released. All analytical data are reported at the confidence level of 1σ (standard deviation). Full $^{40}Ar/^{39}Ar$ analytical data tables are presented in Appendix 2.

APPENDIX 2. $^{40}Ar/^{39}Ar$ Potassium Feldspar Analytical Results

Note: isotope beams in mV, rlsd = released, error in age includes J error, all errors 1 sigma
(^{36}Ar through ^{40}Ar are measured beam intensities, corrected for decay for the age calculations)

Sample RGD17-39, K-spar, 20.01 mg, J = 0.002578 ± 0.57%
4 amu discrimination = 0.8838 ± 0.06%, 40/39K = 0.0429 ± 7.89%, 36/37Ca = 0.0001934 ± 0.59%, 39/37Ca = 0.0005693 ± 0.25%

Step	T (°C)	t (min.)	^{36}Ar	^{37}Ar	^{38}Ar	^{39}Ar	^{40}Ar	$\%^{40}Ar^*$	% ^{39}Ar rlsd	Ca/K	$^{40}Ar^*/^{39}Ar_K$	Age (Ma)	1s.d.
1	422	11	1.860	0.019	0.427	1.590	628.370	1.3	0.1	0.46600838	4.758998	22.00	5.20
2	422	21	0.325	0.010	0.082	0.618	114.456	7.0	0.0	0.63105399	10.615223	48.71	2.96
3	473	10	0.242	0.014	0.073	1.416	109.687	28.9	0.0	0.38556126	20.553958	93.15	0.62
4	473	20	0.112	0.015	0.046	1.383	47.652	40.9	0.0	0.42296235	8.523988	39.22	0.43
5	525	9	0.141	0.013	0.079	3.440	93.504	54.4	0.1	0.14736282	13.351977	61.05	0.56
6	525	20	0.077	0.020	0.073	3.835	50.588	82.0	0.1	0.20336380	6.733456	31.05	0.43
7	576	12	0.180	0.029	0.134	6.274	119.744	54.2	0.2	0.18024367	9.206197	42.32	0.50
8	576	22	0.070	0.024	0.089	5.552	58.887	90.8	0.2	0.16856487	6.124506	28.26	0.38
9	627	12	0.111	0.064	0.170	10.454	114.071	73.6	0.4	0.23873182	7.104620	32.74	0.33
10	627	22	0.065	0.080	0.156	10.570	87.551	96.9	0.4	0.29514395	5.964228	27.53	0.35
11	679	12	0.116	0.111	0.260	17.457	154.628	79.8	0.6	0.24795175	6.452033	29.76	0.21
12	679	22	0.052	0.076	0.206	14.726	111.456	99.3	0.5	0.20125079	6.015099	27.76	0.18
13	730	12	0.095	0.130	0.304	22.655	178.512	86.7	0.8	0.22376415	6.282008	28.98	0.20
14	730	22	0.057	0.124	0.297	22.604	160.738	99.3	0.8	0.21391761	6.014444	27.76	0.17
15	781	13	0.082	0.176	0.409	28.968	216.278	91.0	1.0	0.23692276	6.276109	28.96	0.17
16	781	23	0.048	0.170	0.376	27.696	196.912	99.4	0.9	0.23935624	6.129092	28.28	0.19
17	822	19	0.066	0.221	0.455	34.473	244.096	98.5	1.2	0.24999264	6.281134	28.98	0.20
18	843	19	0.048	0.164	0.379	28.401	204.015	99.4	1.0	0.22517573	6.333358	29.22	0.18
19	884	19	0.065	0.236	0.487	37.454	274.552	98.8	1.3	0.24571257	6.573368	30.32	0.18
20	910	19	0.055	0.188	0.404	29.262	219.942	99.4	1.0	0.25053473	6.673087	30.77	0.18
21	935	19	0.050	0.162	0.310	23.539	180.448	99.2	0.8	0.26837559	6.669588	30.76	0.18
22	961	19	0.070	0.138	0.336	25.203	198.524	97.6	0.9	0.21351921	6.814181	31.42	0.18
23	976	19	0.071	0.088	0.297	20.670	166.607	96.9	0.7	0.16601495	6.708739	30.94	0.19
24	1002	19	0.091	0.084	0.334	24.435	201.130	93.8	0.8	0.13405052	6.769988	31.22	0.18
25	1018	19	0.103	0.058	0.360	25.661	214.602	92.1	0.9	0.08813554	6.799960	31.35	0.18
26	1038	19	0.134	0.050	0.414	29.747	254.806	89.0	1.0	0.06554220	6.829934	31.49	0.20
27	1089	13	0.198	0.066	0.637	46.091	403.100	86.0	1.6	0.05583686	7.047698	32.48	0.22
28	1089	23	0.198	0.071	0.827	58.521	500.195	90.5	2.0	0.04730847	7.138559	32.90	0.19
29	1089	57	0.439	0.094	1.512	106.766	921.629	89.4	3.6	0.03433094	6.991002	32.23	0.19
30	1089	117	0.670	0.125	2.336	163.489	1445.99	91.6	5.5	0.02981342	7.179070	33.08	0.20
31	1192	11	0.656	0.119	2.017	139.558	1263.93	83.0	4.7	0.03324933	7.193305	33.15	0.20
32	1243	11	1.031	0.294	5.054	367.137	3063.73	88.6	12.4	0.03122552	7.119071	32.81	0.19
33	1346	11	1.398	0.713	19.453	1461.913	11673.66	95.7	49.4	0.01901767	7.370515	33.96	0.20
34	1398	11	0.217	0.141	2.124	156.578	1267.68	95.8	5.3	0.03511392	7.333708	33.79	0.20
							Cumulative %39Ar		100.0		Total gas age =	33.09	0.18

Sample RGD17-19, K-spar, 20.80 mg, J = 0.002665 ± 0.55%
4 amu discrimination = 0.9177 ± 0.02%, 40/39K = 0.0429 ± 7.89%, 36/37Ca = 0.0001934 ± 0.59%, 39/37Ca = 0.0005693 ± 0.25%

step	T (C)	t (min.)	^{36}Ar	^{37}Ar	^{38}Ar	^{39}Ar	^{40}Ar	$\%^{40}Ar^*$	% ^{39}Ar rlsd	Ca/K	$^{40}Ar^*/^{39}Ar_K$	Age (Ma)	1s.d.
1	422	11	15.376	0.208	3.400	3.883	5177.52	4.4	0.1	1.06670224	56.962541	254.97	40.79
2	422	21	2.114	0.049	0.498	1.714	730.387	7.0	0.0	0.56921857	28.073716	130.16	5.92
3	473	10	1.125	0.075	0.321	4.416	469.494	23.4	0.1	0.33814359	23.673764	110.37	1.69
4	473	20	0.570	0.044	0.186	4.203	229.271	22.6	0.1	0.20842428	10.741645	50.92	0.57
5	525	9	0.511	0.087	0.248	9.981	264.271	39.6	0.3	0.17353875	9.786701	46.45	0.39
6	525	20	0.277	0.092	0.250	14.337	154.634	50.5	0.4	0.12775441	4.459232	21.31	0.22
7	576	12	0.355	0.193	0.497	32.358	316.502	66.9	0.8	0.11874655	6.082214	29.01	0.18
8	576	22	0.119	0.152	0.399	29.172	151.833	88.9	0.7	0.10373400	3.700426	17.70	0.13
9	627	12	0.257	0.331	0.749	55.733	305.449	77.4	1.4	0.11823904	3.939741	18.84	0.12
10	627	22	0.084	0.300	0.707	53.524	227.240	98.2	1.4	0.11158795	3.591429	17.19	0.11
11	679	12	0.195	0.553	1.018	76.871	366.355	85.0	2.0	0.14322229	3.807564	18.21	0.11
12	679	22	0.097	0.565	0.983	75.298	312.643	95.9	1.9	0.14938730	3.570012	17.08	0.11
13	730	12	0.134	0.836	1.186	90.998	401.685	91.3	2.3	0.18290547	3.801891	18.19	0.11
14	730	22	0.096	0.774	1.051	81.047	351.729	96.6	2.1	0.19013281	3.790336	18.13	0.11
15	781	13	0.129	1.072	1.285	95.369	436.306	92.3	2.4	0.22379183	3.985773	19.06	0.11

16	781	23	0.145	0.913	1.094	82.782	387.830	93.3	2.1	0.21957914	3.974632	19.01	0.11
17	822	19	0.082	1.099	1.267	95.997	429.866	98.1	2.5	0.22792772	4.071965	19.47	0.12
18	843	19	0.068	0.853	1.042	77.549	352.138	99.3	2.0	0.21899237	4.126424	19.73	0.13
19	884	19	0.085	0.921	1.153	89.638	418.074	97.9	2.3	0.20456064	4.223796	20.19	0.12
20	910	19	0.069	0.604	1.028	77.074	367.700	99.2	2.0	0.15601933	4.343705	20.76	0.12
21	935	19	0.078	0.386	0.948	70.365	344.048	98.3	1.8	0.10921316	4.391679	20.99	0.12
22	961	19	0.084	0.294	0.923	70.071	348.363	97.7	1.8	0.08353156	4.443027	21.24	0.12
23	976	19	0.097	0.218	0.870	65.416	339.841	97.4	1.7	0.06634562	4.613534	22.05	0.13
24	1002	19	0.165	0.228	1.016	75.523	413.883	92.2	1.9	0.0601028	4.665122	22.29	0.14
25	1018	19	0.210	0.219	1.068	79.645	452.171	89.5	2.0	0.05474243	4.713558	22.52	0.13
26	1038	19	0.300	0.228	1.308	95.141	568.086	86.3	2.4	0.0477095	4.831726	23.08	0.13
27	1089	13	0.443	0.273	1.850	136.100	859.329	84.3	3.5	0.03993387	5.107805	24.39	0.14
28	1089	23	0.438	0.326	2.025	151.542	929.127	86.5	3.9	0.04282741	5.028544	24.02	0.16
29	1089	57	0.597	0.522	2.935	215.430	1340.04	89.5	5.5	0.04823942	5.161569	24.65	0.14
30	1089	117	0.689	0.700	3.158	231.022	1457.69	92.9	5.9	0.06032312	5.178227	24.73	0.14
31	1192	11	0.514	0.631	2.158	159.130	1086.84	85.0	4.1	0.07894387	5.612852	26.79	0.16
32	1243	11	0.639	1.225	4.041	295.829	2010.87	89.7	7.6	0.08243978	5.922456	28.25	0.16
33	1346	11	2.448	2.992	13.649	1004.87	6973.23	88.3	25.7	0.05927761	5.974222	28.50	0.16
34	1398	11	0.527	1.236	2.767	203.588	1411.41	88.5	5.2	0.12086816	5.924146	28.26	0.17
							Cumulative %39Ar rlsd =		**100.0**		**Total gas age =**	**24.89**	**0.13**

Sample RGD17-21, K-spar, 20.45 mg, J = 0.002637 ± 0.49%

4 amu discrimination = 0.8851 ± 0.04%, 40/39K = 0.0429 ± 7.89%, 36/37Ca = 0.0001934 ± 0.59%, 39/37Ca = 0.0005693 ± 0.25%

step	T (C)	t (min.)	^{36}Ar	^{37}Ar	^{38}Ar	^{39}Ar	^{40}Ar	$\%^{40}Ar^{*}$	% ^{39}Ar rlsd	Ca/K	$^{40}Ar^{*}/^{39}Ar_{K}$	Age (Ma)	1s.d.
1	422	11	2.079	0.018	0.572	7.057	1028.82	33.2	0.2	0.05489741	46.235358	207.55	2.22
2	422	21	0.417	0.014	0.162	4.332	176.267	24.8	0.1	0.06955697	8.313510	39.12	0.55
3	473	10	0.274	0.019	0.221	11.800	206.127	59.2	0.3	0.03465524	9.377630	44.07	0.49
4	473	20	0.138	0.016	0.200	13.220	96.966	76.0	0.3	0.02604863	3.862007	18.28	0.42
5	525	9	0.206	0.023	0.444	29.450	251.332	76.2	0.7	0.01680885	5.990466	28.28	0.17
6	525	20	0.063	0.026	0.377	27.369	129.384	98.5	0.7	0.02044609	3.629351	17.18	0.11
7	576	12	0.136	0.041	0.684	51.051	274.672	88.1	1.3	0.01728523	4.346877	20.56	0.12
8	576	22	0.063	0.029	0.503	37.673	175.735	98.6	0.9	0.01656774	3.753940	17.77	0.12
9	627	12	0.111	0.040	0.780	59.197	318.537	91.3	1.5	0.01454305	4.531255	21.43	0.12
10	627	22	0.053	0.031	0.679	52.634	254.511	98.8	1.3	0.01267624	4.133263	19.56	0.11
11	679	12	0.091	0.042	0.973	72.381	376.184	94.4	1.8	0.01248877	4.574225	21.63	0.12
12	679	22	0.042	0.034	0.838	64.340	312.402	98.9	1.6	0.01137346	4.262268	20.16	0.11
13	730	12	0.084	0.039	1.106	83.814	429.908	95.6	2.1	0.01001481	4.591670	21.71	0.11
14	730	22	0.043	0.033	0.900	69.336	348.142	97.9	1.7	0.01024354	4.568694	21.61	0.11
15	781	13	0.069	0.034	1.164	87.813	451.357	96.9	2.2	0.00833325	4.658904	22.03	0.11
16	781	23	0.049	0.032	1.101	84.711	431.674	99.0	2.1	0.00813026	4.575927	21.64	0.11
17	822	19	0.070	0.040	1.454	110.892	583.913	99.1	2.7	0.00776344	4.854927	22.95	0.12
18	843	19	0.055	0.037	1.318	104.304	537.141	100.0	2.6	0.00763476	4.785957	22.63	0.12
19	884	19	0.096	0.049	2.033	150.480	792.875	98.0	3.7	0.00700828	4.856631	22.96	0.12
20	910	19	0.086	0.046	1.839	143.359	762.212	98.4	3.5	0.00690601	4.915393	23.23	0.12
21	935	19	0.106	0.049	2.045	155.833	854.413	97.7	3.8	0.00676754	5.049773	23.87	0.12
22	961	19	0.172	0.051	2.190	168.038	938.611	95.5	4.1	0.00653216	5.037845	23.81	0.12
23	976	19	0.159	0.051	2.048	156.050	896.667	95.8	3.8	0.00703397	5.192296	24.53	0.12
24	1002	19	0.262	0.057	2.413	181.306	1079.88	93.2	4.5	0.00676639	5.257504	24.84	0.17
25	1018	19	0.269	0.052	2.172	166.116	1016.60	92.6	4.1	0.0067373	5.359813	25.32	0.13
26	1038	19	0.340	0.066	2.165	161.630	1022.97	90.3	4.0	0.00878854	5.406074	25.54	0.13
27	1089	13	0.528	0.084	2.672	196.260	1306.11	87.0	4.8	0.00921175	5.533801	26.14	0.13
28	1089	23	0.448	0.095	2.400	177.620	1189.86	88.8	4.4	0.01151136	5.620397	26.54	0.14
29	1089	57	0.569	0.117	2.837	208.245	1465.31	90.8	5.1	0.01209222	5.892045	27.82	0.14
30	1089	117	0.683	0.126	2.713	196.951	1470.53	93.0	4.8	0.01376916	6.078233	28.69	0.16
31	1192	11	0.544	0.121	1.564	108.816	937.815	81.3	2.7	0.02393254	6.684822	31.53	0.16
32	1243	11	1.441	0.186	4.334	308.665	2560.66	81.1	7.6	0.01296942	6.478030	30.56	0.16
33	1346	11	2.470	0.093	8.050	575.004	4869.06	82.8	14.1	0.00348102	6.766329	31.91	0.16
34	1398	11	0.271	0.022	0.611	42.521	389.559	80.0	1.0	0.01113561	6.795642	32.04	0.19
							Cumulative %39Ar rlsd		100.0		Total gas age	26.45	0.12

Sample RGD18A-6, K-spar, 20.23 mg, J = 0.00171 ± 0.07%

4 amu discrimination = 0.8488 ± 0.02%, 40/39K = 0.0155 ± 22.60%, 36/37Ca = 0.000231 ± 0.77%, 39/37Ca = 0.000637 ± 0.33%

step	T (C)	t (min.)	^{36}Ar	^{37}Ar	^{38}Ar	^{39}Ar	^{40}Ar	$\%^{40}Ar^{*}$	% ^{39}Ar rlsd	Ca/K	$^{40}Ar^{*}/^{39}Ar_{K}$	Age (Ma)	1s.d.
1	422	11	3.221	0.011	0.772	4.744	1405.07	20.4	0.2	0.079567545	57.382269	168.87	1.82
2	422	21	0.933	0.003	0.222	2.362	343.360	6.2	0.1	0.043583836	7.963367	24.40	0.48
3	473	10	0.646	0.012	0.242	5.874	307.510	27.3	0.2	0.070102619	13.123486	40.04	0.21
4	473	20	0.464	0.009	0.209	6.872	226.139	31.6	0.2	0.044941089	8.827797	27.03	0.52
5	525	9	0.414	0.010	0.251	11.203	235.170	40.4	0.4	0.030630096	7.727175	23.68	0.27
6	525	20	0.332	0.008	0.201	10.100	171.416	37.4	0.4	0.027180093	5.166332	15.87	0.28
7	576	12	0.346	0.010	0.300	18.373	237.089	51.9	0.7	0.018676751	5.996555	18.41	0.09
8	576	22	0.174	0.018	0.313	20.384	222.083	83.0	0.7	0.030301614	7.552145	23.15	0.17
9	627	12	0.435	0.029	0.577	36.846	372.621	61.4	1.3	0.027007846	5.696990	17.49	0.09
10	627	22	0.250	0.026	0.443	31.275	263.888	74.7	1.1	0.028527157	5.386127	16.54	0.10
11	679	12	0.461	0.040	0.646	45.281	412.535	63.1	1.6	0.030312841	5.311218	16.31	0.27
12	679	22	0.240	0.030	0.590	42.501	331.149	81.5	1.5	0.024221672	5.580806	17.14	0.07
13	730	12	0.312	0.051	0.725	53.369	416.627	76.3	1.9	0.032791708	5.507835	16.91	0.09
14	730	22	0.198	0.034	0.611	48.094	352.912	87.2	1.7	0.024258840	5.653459	17.36	0.06
15	781	13	0.282	0.048	0.797	50.160	369.518	80.0	1.8	0.032837240	5.526486	16.97	0.04
16	781	23	0.219	0.030	0.684	50.160	369.518	85.6	1.8	0.020523212	5.572298	17.11	0.06
17	822	19	0.209	0.041	0.768	57.824	418.952	88.4	2.1	0.024330876	5.793227	17.78	0.06
18	843	19	0.190	0.037	0.634	48.716	359.738	88.4	1.7	0.026062274	5.846590	17.95	0.09
19	884	19	0.234	0.045	0.848	64.918	488.938	88.3	2.3	0.023786434	6.061398	18.60	0.05
20	910	19	0.155	0.037	0.718	55.752	406.571	93.0	2.0	0.022773151	6.119043	18.78	0.09
21	935	19	0.177	0.036	0.664	53.244	393.182	90.7	1.9	0.023201375	6.029958	18.51	0.06
22	961	19	0.186	0.037	0.719	55.934	429.173	90.7	2.0	0.02269905	6.301186	19.34	0.06
23	976	19	0.187	0.016	0.652	49.489	395.190	88.8	1.8	0.011094095	6.355577	19.50	0.03
24	1002	19	0.269	0.034	0.784	57.193	479.506	84.6	2.0	0.020399411	6.430292	19.73	0.03
25	1018	19	0.287	0.025	0.807	59.598	529.849	84.9	2.1	0.014394258	6.877466	21.09	0.12
26	1038	19	0.360	0.032	0.923	67.494	612.590	82.6	2.4	0.016269191	6.883697	21.11	0.03
27	1089	13	0.646	0.047	1.446	100.577	974.860	78.2	3.6	0.016035419	7.120865	21.84	0.04
28	1089	23	0.678	0.051	1.667	118.753	1098.00	80.3	4.2	0.014736915	6.910263	21.19	0.05
29	1089	57	1.059	0.070	2.470	177.267	1677.47	81.4	6.3	0.013550365	7.040815	21.59	0.03
30	1089	117	1.261	0.082	2.780	200.377	1935.08	83.8	7.1	0.014042580	7.131037	21.87	0.06
31	1192	11	1.061	0.099	1.993	136.291	1502.16	76.3	4.8	0.024925857	7.946939	24.35	0.12
32	1243	11	1.605	0.147	3.730	259.071	2826.06	80.7	9.2	0.019470631	8.362052	25.61	0.09
33	1346	11	4.728	0.124	9.910	700.116	7409.49	78.0	24.9	0.006077595	7.855935	24.07	0.15
34	1398	11	0.795	0.025	1.655	115.216	1267.54	79.9	4.1	0.007445732	8.192750	25.10	0.06
							Cumulative %39Ar rlsd =		**100.0**		**Total gas age =**	**22.10**	**0.02**

APPENDIX 3. Multi-diffusion Domain Model Parameters for Selected Runs

SAMPLE INFO: RGD18A6sph
FILE SUFFIX: 18A6sph

CRS ITERATIONS: 4000
MODEL DURATION (m.y.): 40.0
MC, CRS TIME NODES: 20 40
CONSTRAINING BRACKETS tT: 3
TIME TMIN TMAX
40.0 600.0 750.0
24.0 50.0 500.0
0.0 0.0 50.0
MAX MONTE-CARLO HEATING RATE: 20.0
MAX MONTE-CARLO COOLING RATE: 300.0
MAX CRS HEATING RATE: 40.0
MAX CRS COOLING RATE: 300.0
CRS AMPLIFICATION FACTOR: 1.30
SUBSET SIZE, POOL SIZE: 25 100
FITTING CRITERION: 3.00
FITTING OPTION: 2 (mswd)
DIFFUSION GEOMETRY: 1 (spherical)
RESTART OPTION: 0 (new start from Monte-Carlo histories)
DISCRETIZATION DELTA-TEMPERATURE: 2.0
LOVERA SERIES CUT-OFF: 1.0e-05
FLAG TO WRITE FULL REPORTS: 1
PLOT RESULTS WITH GMT: 2 (will try to make plots)
OF BEST HISTORIES TO PLOT: 15
OF WORST HISTORIES TO PLOT: 15
CUTOFF, EARLY-STEP WEIGHTING: 0.150
EARLY-STEP WEIGHT: 3.0
MAX PERMITTED tT REVERSALS: 1

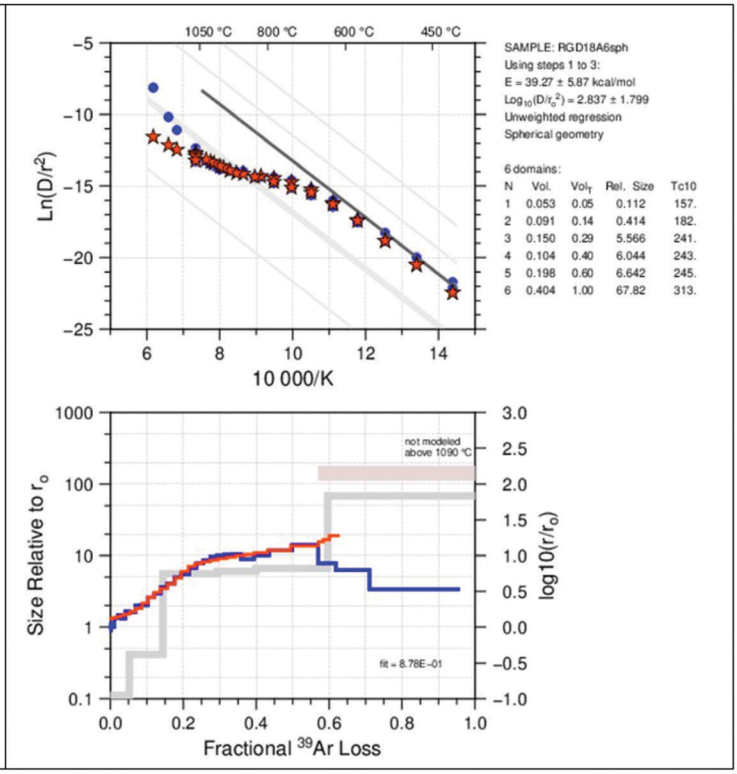

---------- **RGD18-A6 Mineral-Age Info** ----------

NUMBER OF MINERAL AGES: 7

***** MINERAL 1: 3 - other (no alpha loss
GOAL MINERAL AGE 1: 24.00 Ma ERROR IN AGE: 0.50 Ma
MINERAL-AGE WEIGHTING FACTOR 1: 0.50
EFFECTIVE RADIUS 1: 150.00 microns
ACTIVATION ENERGY 1: 47.00 kcal/mol DIFZERO: 7.700e-02 cm2/sec
PARENT CONCENTRATIONS 1: 100.00 ppm U 100.00 ppm Th 0.00 ppm Sm

***** MINERAL 2: 4 - apatite (RDAAM)
GOAL MINERAL AGE 2: 9.60 Ma ERROR IN AGE: 0.75 Ma
MINERAL-AGE WEIGHTING FACTOR 2: 0.50
EFFECTIVE RADIUS 2: 46.00 microns
ACTIVATION ENERGY 2: 46.00 kcal/mol DIFZERO: 7.500e-02 cm2/sec
PARENT CONCENTRATIONS 2: 18.20 ppm U 23.70 ppm Th 0.00 ppm Sm

***** MINERAL 3: 4 - apatite (RDAAM)
GOAL MINERAL AGE 3: 9.70 Ma ERROR IN AGE: 1.40 Ma
MINERAL-AGE WEIGHTING FACTOR 3: 0.50
EFFECTIVE RADIUS 3: 93.00 microns
ACTIVATION ENERGY 3: 46.00 kcal/mol DIFZERO: 7.500e-02 cm2/sec
PARENT CONCENTRATIONS 3: 0.90 ppm U 1.30 ppm Th 0.00 ppm Sm

***** MINERAL 4: 4 - apatite (RDAAM)
GOAL MINERAL AGE 4: 6.60 Ma ERROR IN AGE: 1.00 Ma
MINERAL-AGE WEIGHTING FACTOR 4: 0.50
EFFECTIVE RADIUS 4: 73.00 microns
ACTIVATION ENERGY 4: 46.00 kcal/mol DIFZERO: 7.500e-02 cm2/sec
PARENT CONCENTRATIONS 4: 1.90 ppm U 2.00 ppm Th 0.00 ppm Sm

***** MINERAL 5: 4 - apatite (RDAAM)
GOAL MINERAL AGE 5: 7.10 Ma ERROR IN AGE: 2.00 Ma
MINERAL-AGE WEIGHTING FACTOR 5: 0.50
EFFECTIVE RADIUS 5: 70.00 microns
ACTIVATION ENERGY 5: 46.00 kcal/mol DIFZERO: 7.500e-02 cm2/sec
PARENT CONCENTRATIONS 5: 1.10 ppm U 1.00 ppm Th 0.00 ppm Sm

***** MINERAL 6: 4 - apatite (RDAAM)
GOAL MINERAL AGE 6: 6.60 Ma ERROR IN AGE: 7.10 Ma
MINERAL-AGE WEIGHTING FACTOR 6: 0.50
EFFECTIVE RADIUS 6: 56.00 microns
ACTIVATION ENERGY 6: 46.00 kcal/mol DIFZERO: 7.500e-02 cm2/sec
PARENT CONCENTRATIONS 6: 0.40 ppm U 0.60 ppm Th 0.00 ppm Sm

***** MINERAL 7: 4 - apatite (RDAAM)
GOAL MINERAL AGE 7: 5.60 Ma ERROR IN AGE: 1.20 Ma
MINERAL-AGE WEIGHTING FACTOR 7: 0.50
EFFECTIVE RADIUS 7: 65.00 microns
ACTIVATION ENERGY 7: 46.00 kcal/mol DIFZERO: 7.500e-02 cm2/sec
PARENT CONCENTRATIONS 7: 1.50 ppm U 1.20 ppm Th 0.00 ppm Sm
DIFFUSION and RDAAM PRECISION? 1 - better
ARE MINERAL AGES CONSTRAINTS? 1 – yes

RGD18-A6 DOMAIN INFO

Domains: 6

	E	D0	frac.
1	39.27	1.72705e+18	0.053
2	39.27	1.26417e+17	0.091
3	39.27	7.00171e+14	0.150
4	39.27	5.93614e+14	0.104
5	39.27	4.91478e+14	0.198
6	39.27	4.71416e+12	0.404

********* Arvert 6.1.1 finished with no worries! **********
Processed 4000 CRS histories
in 5.88 minutes at a rate of 0.147 minutes per 100 histories
Best fit is 59.26, worst fit is 59.64

Goal spectrum steps: 33

	f39	age	error	skip?
1	0.002	168.9	1.8	0
2	0.003	24.4	0.5	0
3	0.005	40.0	0.2	0
4	0.007	27.0	0.5	0
5	0.011	23.7	0.3	0
6	0.015	15.9	0.3	0
7	0.021	18.4	0.1	0
8	0.028	23.1	0.2	0
9	0.041	17.5	0.1	0
10	0.053	16.5	0.1	1
11	0.069	16.3	0.3	0
12	0.084	17.1	0.1	1
13	0.103	16.9	0.1	0
14	0.120	17.4	0.1	1
15	0.138	17.0	0.0	0
16	0.155	17.1	0.1	1
17	0.176	17.8	0.1	1
18	0.193	17.9	0.1	1
19	0.216	18.6	0.1	1
20	0.236	18.8	0.1	1
21	0.255	18.5	0.1	1
22	0.275	19.3	0.1	1
23	0.292	19.5	0.0	1
24	0.313	19.7	0.0	1
25	0.334	21.1	0.1	1
26	0.358	21.1	0.0	1
27	0.394	21.8	0.0	1
28	0.436	21.2	0.1	1
29	0.499	21.6	0.0	1
30	0.570	21.9	0.1	1
31	0.618	24.4	0.1	0
32	0.710	25.6	0.1	0
33	0.959	24.1	0.1	0

Heating Schedule Actually Used – 33 Heating Steps:

	Temp. (C)	Time
1	442.6	10.0
2	448.4	10.0
3	488.7	10.0
4	508.8	10.0
5	539.2	10.0
6	548.4	10.0
7	582.9	10.0
8	600.9	10.0
9	642.5	10.0
10	652.7	10.0
11	688.2	10.0
12	705.7	10.0
13	744.4	10.0
14	770.6	10.0
15	799.8	10.0
16	824.7	10.0
17	859.7	10.0
18	881.6	10.0
19	942.9	10.0
20	967.7	10.0
21	985.3	10.0
22	1005.7	10.0
23	1011.5	10.0
24	1037.8	10.0
25	1055.3	10.0
26	1081.6	10.0
27	1142.9	10.0
28	1189.6	10.0
29	1274.3	10.0
30	1359.0	10.0
31	1394.0	10.0
32	1797.0	10.0
33	2883.2	10.0

Arvert 6.1.1 model run Fri Jan 17 12:44:23 2020

SAMPLE INFO: RGD17-19

FILE SUFFIX: RGD1719slabBtAp

CRS ITERATIONS: 7500
MODEL DURATION (m.y.): 40.0
MC, CRS TIME NODES: 20 40
CONSTRAINING BRACKETS tT: 4
TIME TMIN TMAX
40.0 600.0 750.0
25.0 50.0 500.0
10.0 15.0 150.0
0.0 0.0 50.0
MAX MONTE-CARLO HEATING RATE: 10.0
MAX MONTE-CARLO COOLING RATE: 100.0
MAX CRS HEATING RATE: 20.0
MAX CRS COOLING RATE: 200.0
CRS AMPLIFICATION FACTOR: 1.50
SUBSET SIZE, POOL SIZE: 30 250
FITTING CRITERION: 3.00
FITTING OPTION: 2 (mswd)
DIFFUSION GEOMETRY: 2 (infinite-slab)
RESTART OPTION: 0 (new start from Monte-Carlo histories)
DISCRETIZATION DELTA-TEMPERATURE: 2.0
LOVERA SERIES CUT-OFF: 1.0e-07
FLAG TO WRITE FULL REPORTS: 1
PLOT RESULTS WITH GMT: 2 (will try to make plots)
OF BEST HISTORIES TO PLOT: 15
OF WORST HISTORIES TO PLOT: 15
CUTOFF, EARLY-STEP WEIGHTING: 0.150
EARLY-STEP WEIGHT: 3.0
MAX PERMITTED tT REVERSALS: 1

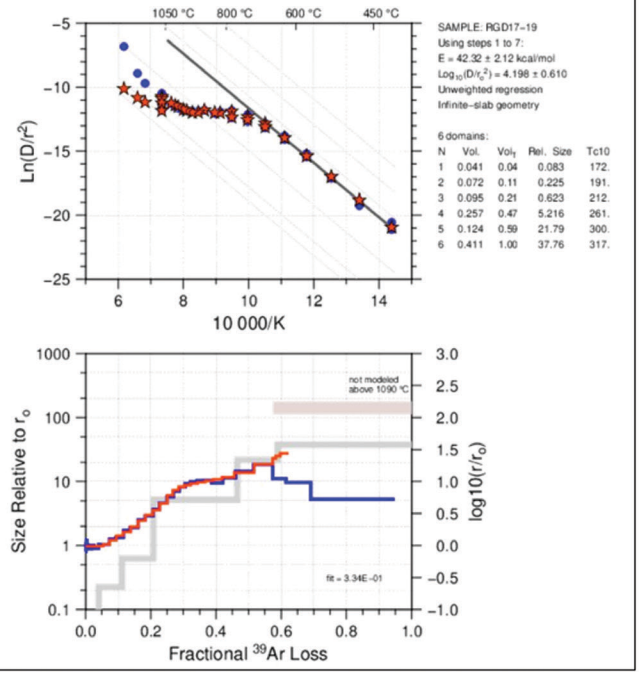

---------- RGD17-9 Mineral-Age Info ----------

NUMBER OF MINERAL AGES: 4

***** MINERAL 1: 3 - other (no alpha loss
GOAL MINERAL AGE 1: 25.40 Ma ERROR IN AGE: 1.00 Ma
MINERAL-AGE WEIGHTING FACTOR 1: 1.00
EFFECTIVE RADIUS 1: 150.00 microns
ACTIVATION ENERGY 1: 47.00 kcal/mol DIFZERO: 7.700e-01 cm2/sec
PARENT CONCENTRATIONS 1: 100.00 ppm U 100.00 ppm Th 0.00 ppm Sm

***** MINERAL 2: 4 - apatite (RDAAM)
GOAL MINERAL AGE 2: 12.94 Ma ERROR IN AGE: 1.00 Ma
MINERAL-AGE WEIGHTING FACTOR 2: 1.00
EFFECTIVE RADIUS 2: 78.00 microns
ACTIVATION ENERGY 2: 46.00 kcal/mol DIFZERO: 7.500e-03 cm2/sec
PARENT CONCENTRATIONS 2: 0.10 ppm U 9.70 ppm Th 0.00 ppm Sm

***** MINERAL 3: 4 - apatite (RDAAM)
GOAL MINERAL AGE 3: 11.50 Ma ERROR IN AGE: 2.10 Ma
MINERAL-AGE WEIGHTING FACTOR 3: 1.00
EFFECTIVE RADIUS 3: 48.00 microns
ACTIVATION ENERGY 3: 46.00 kcal/mol DIFZERO: 7.500e-03 cm2/sec
PARENT CONCENTRATIONS 3: 0.20 ppm U 20.70 ppm Th 0.00 ppm Sm

***** MINERAL 4: 4 - apatite (RDAAM)
GOAL MINERAL AGE 4: 12.65 Ma ERROR IN AGE: 3.90 Ma
MINERAL-AGE WEIGHTING FACTOR 4: 1.00
EFFECTIVE RADIUS 4: 63.00 microns
ACTIVATION ENERGY 4: 46.00 kcal/mol DIFZERO: 7.500e-03 cm2/sec
PARENT CONCENTRATIONS 4: 12.30 ppm U 21.10 ppm Th 0.00 ppm Sm
DIFFUSION and RDAAM PRECISION?: 1 - better
ARE MINERAL AGES CONSTRAINTS?: 1 – yes

RGD17-19 DOMAIN INFO

Domains: 6

	E	D0	frac.
1	42.32	7.28960e+19	0.041
2	42.32	9.84927e+18	0.072
3	42.32	1.28146e+18	0.095
4	42.32	1.82938e+16	0.257
5	42.32	1.04834e+15	0.124
6	42.32	3.48983e+14	0.411

****
Arvert 6.1.1 finished with no worries
****

Processed 7500 CRS histories
in 6.82 minutes at a rate of 0.091 minutes per 100 histories
Best fit is 14.86, worst fit is 18.03

Goal Age Spectrum

Goal spectrum steps: 33

	f39	age	error	skip?
1	0.001	255.0	40.8	0
2	0.001	130.2	5.9	0
3	0.003	110.4	1.7	0
4	0.004	50.9	0.6	0
5	0.006	46.5	0.4	0
6	0.010	21.3	0.2	0
7	0.018	29.0	0.2	0
8	0.026	17.7	0.1	0
9	0.040	18.8	0.1	0
10	0.054	17.2	0.1	0
11	0.073	18.2	0.1	0
12	0.093	17.1	0.1	1
13	0.116	18.2	0.1	1
14	0.137	18.1	0.1	1
15	0.161	19.1	0.1	1
16	0.182	19.0	0.1	1
17	0.207	19.5	0.1	1
18	0.227	19.7	0.1	1
19	0.250	20.2	0.1	1
20	0.269	20.8	0.1	1
21	0.287	21.0	0.1	1
22	0.305	21.2	0.1	1
23	0.322	22.1	0.1	1
24	0.341	22.3	0.1	1
25	0.362	22.5	0.1	1
26	0.386	23.1	0.1	1
27	0.421	24.4	0.1	1
28	0.460	24.0	0.2	1
29	0.515	24.6	0.1	1
30	0.574	24.7	0.1	1
31	0.615	26.8	0.2	0
32	0.691	28.2	0.2	0
33	0.948	28.5	0.2	0

Heating Schedule Actually Used

Heating Steps: 33

	Temp. (C)	Time
1	432.4	10.0
2	434.1	10.0
3	469.7	10.0
4	480.1	10.0
5	517.0	10.0
6	542.9	10.0
7	588.1	10.0
8	600.2	10.0
9	639.2	10.0
10	653.1	10.0
11	685.6	10.0
12	708.6	10.0
13	744.4	10.0
14	761.9	10.0
15	797.6	10.0
16	823.2	10.0
17	862.6	10.0
18	877.2	10.0
19	922.5	10.0
20	959.0	10.0
21	988.2	10.0
22	1008.6	10.0
23	1017.4	10.0
24	1040.7	10.0
25	1058.3	10.0
26	1084.5	10.0
27	1137.1	10.0
28	1169.2	10.0
29	1251.0	10.0
30	1344.4	10.0
31	1394.0	10.0
32	1551.7	10.0
33	2036.4	10.0

Arvert 6.1.1 model run Mon Jan 20 13:48:46 2020

SAMPLE INFO: RGD17_21_sph

FILE SUFFIX: RGD1721_sph

CRS ITERATIONS: 5000
MODEL DURATION (m.y.): 40.0
MC, CRS TIME NODES: 20 40
CONSTRAINING BRACKETS tT: 4
TIME TMIN TMAX
40.0 550.0 800.0
32.0 200.0 650.0
14.0 20.0 150.0
0.0 0.0 50.0
MAX MONTE-CARLO HEATING RATE: 25.0
MAX MONTE-CARLO COOLING RATE: 100.0
MAX CRS HEATING RATE: 25.0
MAX CRS COOLING RATE: 200.0
CRS AMPLIFICATION FACTOR: 1.40
SUBSET SIZE, POOL SIZE: 30 90
FITTING CRITERION: 3.00
FITTING OPTION: 2 (mswd)
DIFFUSION GEOMETRY: 1 (spherical)
RESTART OPTION: 0 (new start from Monte-Carlo histories)
DISCRETIZATION DELTA-TEMPERATURE: 1.0
LOVERA SERIES CUT-OFF: 1.0e-07
FLAG TO WRITE FULL REPORTS: 1
PLOT RESULTS WITH GMT: 2 (will try to make plots)
OF BEST HISTORIES TO PLOT: 15
OF WORST HISTORIES TO PLOT: 15
CUTOFF, EARLY-STEP WEIGHTING: 0.150
EARLY-STEP WEIGHT: 3.0
MAX PERMITTED tT REVERSALS: 1

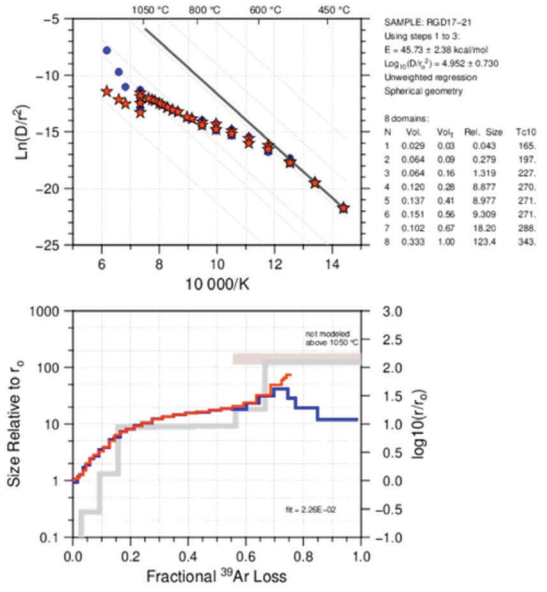

---------- RGD17-21 Mineral-Age Info ----------

NUMBER OF MINERAL AGES: 16

***** MINERAL 1: 4 - apatite (RDAAM)
GOAL MINERAL AGE 1: 11.20 Ma ERROR IN AGE: 1.00 Ma
MINERAL-AGE WEIGHTING FACTOR 1: 1.00
EFFECTIVE RADIUS 1: 64.00 microns
ACTIVATION ENERGY 1: 46.00 kcal/mol DIFZERO: 7.500e-02 cm²/sec
PARENT CONCENTRATIONS 1:
15.20 ppm U 21.20 ppm Th 0.00 ppm Sm

***** MINERAL 2: 4 - apatite (RDAAM)
GOAL MINERAL AGE 2: 10.60 Ma ERROR IN AGE: 1.00 Ma
MINERAL-AGE WEIGHTING FACTOR 2: 1.00
EFFECTIVE RADIUS 2: 64.00 microns
ACTIVATION ENERGY 2: 46.00 kcal/mol DIFZERO: 7.500e-02 cm²/sec
PARENT CONCENTRATIONS 2:
8.30 ppm U 12.70 ppm Th 0.00 ppm Sm

***** MINERAL 3: 4 - apatite (RDAAM)
GOAL MINERAL AGE 3: 9.90 Ma ERROR IN AGE: 0.50 Ma
MINERAL-AGE WEIGHTING FACTOR 3: 1.00
EFFECTIVE RADIUS 3: 63.00 microns
ACTIVATION ENERGY 3: 46.00 kcal/mol DIFZERO: 7.500e-02 cm²/sec
PARENT CONCENTRATIONS 3:
8.80 ppm U 17.40 ppm Th 0.00 ppm Sm

***** MINERAL 4: 4 - apatite (RDAAM)
GOAL MINERAL AGE 4: 10.20 Ma ERROR IN AGE: 1.10 Ma
MINERAL-AGE WEIGHTING FACTOR 4: 1.00
EFFECTIVE RADIUS 4: 52.00 microns
ACTIVATION ENERGY 4: 46.00 kcal/mol DIFZERO: 7.500e-02 cm²/sec
PARENT CONCENTRATIONS 4:
7.80 ppm U 9.60 ppm Th 0.00 ppm Sm

***** MINERAL 5: 4 - apatite (RDAAM)
GOAL MINERAL AGE 5: 9.20 Ma ERROR IN AGE: 0.80 Ma
MINERAL-AGE WEIGHTING FACTOR 5: 1.00
EFFECTIVE RADIUS 5: 48.00 microns
ACTIVATION ENERGY 5: 46.00 kcal/mol DIFZERO: 7.500e-02 cm²/sec
PARENT CONCENTRATIONS 5:
13.60 ppm U 16.10 ppm Th 0.00 ppm Sm

***** MINERAL 9: 4 - apatite (RDAAM)
GOAL MINERAL AGE 9: 8.90 Ma ERROR IN AGE: 0.50 Ma
MINERAL-AGE WEIGHTING FACTOR 9: 1.00
EFFECTIVE RADIUS 9: 62.00 microns
ACTIVATION ENERGY 9: 46.00 kcal/mol DIFZERO: 7.500e-02 cm²/sec
PARENT CONCENTRATIONS 9:
12.60 ppm U 24.00 ppm Th 0.00 ppm Sm

***** MINERAL 10: 4 - apatite (RDAAM)
GOAL MINERAL AGE 10: 10.20 Ma ERROR IN AGE: 0.50 Ma
MINERAL-AGE WEIGHTING FACTOR 10: 1.00
EFFECTIVE RADIUS 10: 61.00 microns
ACTIVATION ENERGY 10: 46.00 kcal/mol DIFZERO: 7.500e-02 cm²/sec
PARENT CONCENTRATIONS 10:
9.30 ppm U 16.10 ppm Th 0.00 ppm Sm

***** MINERAL 11: 5 - zircon (ZRDAAM)
GOAL MINERAL AGE 11: 17.00 Ma ERROR IN AGE: 1.00 Ma
MINERAL-AGE WEIGHTING FACTOR 11: 1.00
EFFECTIVE RADIUS 11: 77.00 microns
ACTIVATION ENERGY 11: 46.00 kcal/mol DIFZERO: 7.500e-02 cm²/sec
PARENT CONCENTRATIONS 11:
747.40 ppm U 242.80 ppm Th 0.00 ppm Sm

***** MINERAL 12: 5 - zircon (ZRDAAM)
GOAL MINERAL AGE 12: 13.60 Ma ERROR IN AGE: 1.00 Ma
MINERAL-AGE WEIGHTING FACTOR 12: 1.00
EFFECTIVE RADIUS 12: 76.30 microns
ACTIVATION ENERGY 12: 46.00 kcal/mol DIFZERO: 7.500e-02 cm²/sec
PARENT CONCENTRATIONS 12:
406.10 ppm U 124.40 ppm Th 1.00 ppm Sm

***** MINERAL 13: 2 - titanite (volume diffusion)
GOAL MINERAL AGE 13: 17.70 Ma ERROR IN AGE: 1.00 Ma
MINERAL-AGE WEIGHTING FACTOR 13: 1.00
EFFECTIVE RADIUS 13: 131.00 microns
ACTIVATION ENERGY 13: 38.50 kcal/mol DIFZERO: 7.433e-01 cm²/sec
PARENT CONCENTRATIONS 13:
172.60 ppm U 205.10 ppm Th 6.10 ppm Sm

***** MINERAL 6: 4 - apatite (RDAAM)
GOAL MINERAL AGE 6: 11.10 Ma ERROR IN AGE: 1.20 Ma
MINERAL-AGE WEIGHTING FACTOR 6: 1.00
EFFECTIVE RADIUS 6: 69.00 microns
ACTIVATION ENERGY 6: 46.00 kcal/mol DIFZERO: 7.500e-02 cm²/sec
PARENT CONCENTRATIONS 6:
11.00 ppm U 16.00 ppm Th 0.00 ppm Sm

***** MINERAL 7: 4 - apatite (RDAAM)
GOAL MINERAL AGE 7: 10.70 Ma ERROR IN AGE: 1.30 Ma
MINERAL-AGE WEIGHTING FACTOR 7: 1.00
EFFECTIVE RADIUS 7: 72.00 microns
ACTIVATION ENERGY 7: 46.00 kcal/mol DIFZERO: 7.500e-02 cm²/sec
PARENT CONCENTRATIONS 7:
12.30 ppm U 19.50 ppm Th 0.00 ppm Sm

***** MINERAL 8: 4 - apatite (RDAAM)
GOAL MINERAL AGE 8: 8.30 Ma ERROR IN AGE: 0.90 Ma
MINERAL-AGE WEIGHTING FACTOR 8: 1.00
EFFECTIVE RADIUS 8: 51.00 microns
ACTIVATION ENERGY 8: 46.00 kcal/mol DIFZERO: 7.500e-02 cm²/sec
PARENT CONCENTRATIONS 8:
11.80 ppm U 18.40 ppm Th 0.00 ppm Sm

***** MINERAL 14: 2 - titanite (volume diffusion)
GOAL MINERAL AGE 14: 20.60 Ma ERROR IN AGE: 1.00 Ma
MINERAL-AGE WEIGHTING FACTOR 14: 1.00
EFFECTIVE RADIUS 14: 150.20 microns
EACTIVATION ENERGY 14: 38.50 kcal/mol DIFZERO: 7.433e-01cm²/sec
PARENT CONCENTRATIONS 14:
117.90 ppm U 197.20 ppm Th 3.00 ppm Sm

***** MINERAL 15: 2 - titanite (volume diffusion)
GOAL MINERAL AGE 15: 19.70 Ma ERROR IN AGE: 1.00 Ma
MINERAL-AGE WEIGHTING FACTOR 15: 1.00
EFFECTIVE RADIUS 15: 66.40 microns
ACTIVATION ENERGY 15: 38.50 kcal/mol DIFZERO: 7.433e-01 cm²/sec
PARENT CONCENTRATIONS 15:
378.60 ppm U 461.60 ppm Th 10.00 ppm Sm

***** MINERAL 16: 3 - other (no alpha loss
GOAL MINERAL AGE 16: 31.35 Ma ERROR IN AGE: 1.00 Ma
MINERAL-AGE WEIGHTING FACTOR 16: 1.00
EFFECTIVE RADIUS 16: 150.00 microns
ACTIVATION ENERGY 16: 47.00 kcal/mol DIFZERO: 7.700e-01 cm²/sec
PARENT CONCENTRATIONS 16:
378.60 ppm U 461.60 ppm Th 10.00 ppm Sm

DIFFUSION and RDAAM PRECISION?: 1 - better
ARE MINERAL AGES CONSTRAINTS?: 1 – yes

RGD17-21 DOMAIN INFO

Domains: 10

	E	D0	frac.
1	45.68	2.08595e+24	0.020
2	45.68	1.01415e+23	0.031
3	45.68	1.07153e+22	0.051
4	45.68	1.05246e+21	0.043
5	45.68	2.17873e+20	0.054
6	45.68	2.50383e+19	0.218
7	45.68	9.55661e+18	0.095
8	45.68	1.62369e+18	0.073
9	45.68	1.58418e+18	0.110
10	45.68	6.91200e+17	0.305

Goal Age Spectrum

Goal spectrum steps: 33

	f39	age	error	skip?
1	0.002	207.6	2.2	0
2	0.003	39.1	0.6	0
3	0.006	44.1	0.5	0
4	0.009	18.3	0.4	0
5	0.016	28.3	0.2	0
6	0.023	17.2	0.1	1
7	0.035	20.6	0.1	0
8	0.045	17.8	0.1	1
9	0.059	21.4	0.1	0
10	0.072	19.6	0.1	1
11	0.090	21.6	0.1	0
12	0.106	20.2	0.1	1
13	0.126	21.7	0.1	1
14	0.143	21.6	0.1	1
15	0.165	22.0	0.1	1
16	0.186	21.6	0.1	1
17	0.213	22.9	0.1	1
18	0.239	22.6	0.1	1
19	0.276	23.0	0.1	1
20	0.311	23.2	0.1	1
21	0.349	23.9	0.1	1
22	0.391	23.8	0.1	1
23	0.429	24.5	0.1	1
24	0.474	24.8	0.2	1
25	0.514	25.3	0.1	1
26	0.554	25.5	0.1	1
27	0.602	26.1	0.1	1
28	0.646	26.5	0.1	1
29	0.697	27.8	0.1	1
30	0.746	28.7	0.2	0
31	0.772	31.5	0.2	0
32	0.848	30.6	0.2	0
33	0.990	31.9	0.2	0

Heating Schedule Actually Used

Heating Steps: 33

	Temp. (C)	Time
1	307.0	10.0
2	314.3	10.0
3	340.4	10.0
4	352.3	10.0
5	377.9	10.0
6	387.8	10.0
7	414.2	10.0
8	424.4	10.0
9	450.4	10.0
10	460.4	10.0
11	481.6	10.0
12	494.3	10.0
13	516.2	10.0
14	524.3	10.0
15	545.1	10.0
16	560.0	10.0
17	582.3	10.0
18	592.5	10.0
19	619.5	10.0
20	633.4	10.0
21	649.5	10.0
22	667.0	10.0
23	677.2	10.0
24	696.2	10.0
25	704.9	10.0
26	715.9	10.0
27	740.0	10.0
28	754.6	10.0
29	783.8	10.0
30	807.1	10.0
31	792.5	10.0
32	872.8	10.0
33	1017.4	10.0

****
Arvert 6.1.1 finished with no worries!
****

Processed 5000 CRS histories
in 12.60 minutes at a rate of 0.252 minutes
per 100 histories

Best fit is 4.46, worst fit is 6.22

PARENT CONCENTRATIONS 5:
2075.60 ppm U 418.70 ppm Th 1.00 ppm Sm

***** MINERAL 6: 5 - zircon (ZRDAAM)
GOAL MINERAL AGE 6: 19.10 Ma ERROR IN AGE: 1.00 Ma
MINERAL-AGE WEIGHTING FACTOR 6: 1.00
EFFECTIVE RADIUS 6: 67.00 microns
ACTIVATION ENERGY 6: 46.00 kcal/mol DIFZERO: 7.500e-02 cm²/sec
PARENT CONCENTRATIONS 6:
633.40 ppm U 227.00 ppm Th 1.00 ppm Sm

***** MINERAL 7: 2 - titanite (volume diffusion)
GOAL MINERAL AGE 7: 25.00 Ma ERROR IN AGE: 1.00 Ma
MINERAL-AGE WEIGHTING FACTOR 7: 1.00
EFFECTIVE RADIUS 7: 97.40 microns
ACTIVATION ENERGY 7: 38.50 kcal/mol DIFZERO: 7.433e-01 cm²/sec
PARENT CONCENTRATIONS 7:
167.00 ppm U 296.00 ppm Th 10.40 ppm Sm

***** MINERAL 8: 2 - titanite (volume diffusion)
GOAL MINERAL AGE 8: 18.60 Ma ERROR IN AGE: 1.00 Ma
MINERAL-AGE WEIGHTING FACTOR 8: 1.00
EFFECTIVE RADIUS 8: 73.20 microns
ACTIVATION ENERGY 8: 38.50 kcal/mol DIFZERO: 7.433e-01 cm²/sec
PARENT CONCENTRATIONS 8:
240.60 ppm U 268.00 ppm Th 29.00 ppm Sm

ACTIVATION ENERGY 13: 46.00 kcal/mol DIFZERO: 7.500e-02 cm²/sec
PARENT CONCENTRATIONS 13:
8.10 ppm U 11.30 ppm Th 0.00 ppm Sm

***** MINERAL 14: 4 - apatite (RDAAM)
GOAL MINERAL AGE 14: 16.60 Ma ERROR IN AGE: 1.00 Ma
MINERAL-AGE WEIGHTING FACTOR 14: 1.00
EFFECTIVE RADIUS 14: 54.00 microns
ACTIVATION ENERGY 14: 46.00 kcal/mol DIFZERO: 7.500e-02 cm²/sec
PARENT CONCENTRATIONS 14:
12.60 ppm U 18.20 ppm Th 0.00 ppm Sm

***** MINERAL 15: 4 - apatite (RDAAM)
GOAL MINERAL AGE 15: 21.80 Ma ERROR IN AGE: 1.70 Ma
MINERAL-AGE WEIGHTING FACTOR 15: 1.00
EFFECTIVE RADIUS 15: 57.00 microns
ACTIVATION ENERGY 15: 46.00 kcal/mol DIFZERO: 7.500e-02 cm²/sec
PARENT CONCENTRATIONS 15:
10.80 ppm U 15.70 ppm Th 0.00 ppm Sm

DIFFUSION and RDAAM PRECISION?: 1 - better

ARE MINERAL AGES CONSTRAINTS?: 1 – yes

RGD17-39 DOMAIN INFO

Domains: 7

	E	D0	frac.
1	42.92	1.07970e+19	0.012
2	42.92	4.49060e+17	0.061
3	42.92	1.44412e+14	0.154
4	42.92	1.34618e+14	0.162
5	42.92	1.15506e+14	0.085
6	42.92	1.08644e+14	0.220
7	42.92	2.32276e+13	0.306

Goal Age Spectrum

Goal spectrum steps: 33

	f39	age	error	skip?
1	0.001	22.0	5.2	0
2	0.001	48.7	3.0	0
3	0.001	93.2	0.6	0
4	0.002	39.2	0.4	0
5	0.003	61.0	0.6	0
6	0.004	31.1	0.4	0
7	0.006	42.3	0.5	0
8	0.008	28.3	0.4	0
9	0.012	32.7	0.3	0
10	0.015	27.5	0.3	1
11	0.021	29.8	0.2	0
12	0.026	27.8	0.2	1
13	0.034	29.0	0.2	0
14	0.041	27.8	0.2	1
15	0.051	29.0	0.2	0
16	0.061	28.3	0.2	1
17	0.072	29.0	0.2	1
18	0.082	29.2	0.2	1
19	0.095	30.3	0.2	1
20	0.104	30.8	0.2	1
21	0.112	30.8	0.2	1
22	0.121	31.4	0.2	1
23	0.128	30.9	0.2	1
24	0.136	31.2	0.2	1
25	0.145	31.4	0.2	1
26	0.155	31.5	0.2	1
27	0.170	32.5	0.2	1
28	0.190	32.9	0.2	1
29	0.226	32.2	0.2	0
30	0.282	33.1	0.2	0
31	0.453	32.8	0.2	0
32	0.947	34.0	0.2	0
33	1.000	33.8	0.2	0

Heating Schedule Actually Used

Heating Steps: 33

	Temp. (C)	Time
1	461.6	10.0
2	459.9	10.0
3	492.7	10.0
4	503.1	10.0
5	543.3	10.0
6	561.0	10.0
7	591.6	10.0
8	599.8	10.0
9	637.1	10.0
10	652.0	10.0
11	689.6	10.0
12	699.8	10.0
13	740.3	10.0
14	764.8	10.0
15	801.3	10.0
16	821.7	10.0
17	858.2	10.0
18	875.8	10.0
19	937.1	10.0
20	973.6	10.0
21	991.1	10.0
22	1011.5	10.0
23	1011.5	10.0
24	1034.9	10.0
25	1049.5	10.0
26	1072.9	10.0
27	1126.9	10.0
28	1166.3	10.0
29	1255.3	10.0
30	1344.4	10.0
31	1591.9	10.0
32	2369.3	10.0
33	2813.1	10.0

****
Arvert 6.1.1 finished with no worries!
****

Processed 2500 CRS histories
in 13.20 minutes at a rate of 0.528
minutes per 100 histories

Best fit is 6.49, worst fit is 6.85